Comprehensive profiling of *N*^{6}-methyladnosine (m^{6}A) readouts reveals novel m^{6}A readers that regulate human embryonic stem cell differentiation

Zhou Huang[1,2,3,4,5,#], Rucong Liu[1,2,3,6,#], Zibaguli Wubulikasimu[3,7,#], Wanqing Zhao[1,2,8,#], Jiaqi Huang[2,4], Jiaxuan Wang[3], Rui Fan[1,2], Wei Kong[2,4], Qinghua Cui[1,2], Yang Li[3,*], Yuan Zhou[1,2,9,*]

[1] Department of Biomedical Informatics, School of Basic Medical Sciences, Peking University, Beijing 100191, China.

[2] State Key Laboratory of Vascular Homeostasis and Remodeling, Peking University, Beijing 100191, China.

[3] Department of Cell Biology, School of Basic Medical Sciences, Peking University Stem Cell Research Center, Peking University, Beijing 100191, China.

[4] Department of Physiology and Pathophysiology, School of Basic Medical Sciences, Peking University, Beijing 100191, China.

[5] Cancer Center, Daping Hospital, Army Medical University, Chongqing 400042, China.

[6] National Institute of Geriatrics, National Health Commission, Beijing Hospital, Beijing 100730, China.

[7] State Key Laboratory of Female Fertility Promotion, Center for Reproductive Medicine, Department of Obstetrics and Gynecology, Peking University Third Hospital, Beijing 100191, China.

[8] Shenzhen Key Laboratory of Cardiovascular Disease, Fuwai Hospital Chinese Academy of Medical Sciences, Shenzhen 518057, China.

[9] Department of Integrated Traditional Chinese and Western Medicine, School of Basic Medical Sciences, Peking University, Beijing 100191, China.

* Correspondence authors: Yuan Zhou (zhouyuanbioinfo@hsc.pku.edu.cn) and Yang Li (liyang@hsc.pku.edu.cn)

# Contributed equally.

Abstract

N^6-methyladenosine (m^{6}A) methylation has emerged as a prevalent RNA modification that extensively impacts various physiological and pathological processes via various post-transcriptional readout effects in mammals. High-throughput methylome profiling has outlined the landscape of m^{6}A modification sites, but their downstream readouts require comprehensive investigation. To this end, we systematically assessed the effects of m^{6}A on mRNA half-life, translation efficiency, and alternative splicing across five cell lines (A549, HEK293T, HUVEC, JURKAT, and human embryonic stem cells (hESCs)) using actinomycin D-disrupted temporal transcriptome sequencing, ribosome sequencing, and ultra-high-depth transcriptome sequencing, respectively. Our analysis, coupled with the integration of public and re-profiled m^{6}A methylome data, revealed high cell type specificity in m^{6}A readouts where m^{6}A level alone is insufficient to predict m^{6}A readouts. Machine learning models focused on the RNA binding protein (RBP) binding context of m^{6}A sites demonstrated substantial predictive ability of m^{6}A readouts while prioritizing putative m^{6}A readers from their informative RBP features. Four novel m^{6}A readers (DDX6, FUBP3, FXR2, and L1TD1) were identified and validated through m^{6}A RNA pull-down assays and transcriptome-wide RBP binding site mapping. Notably, FUBP3, FXR2 and L1TD1 were found to regulate hESC differentiation without impairing self-renewal, underscoring their critical roles in stem cell biology. Together, this study bridges the gap in understanding m^{6}A functional readouts and lays the groundwork for future research on m^{6}A-mediated stem cell fate decisions.

Introduction

The mammalian transcriptome is extensively regulated by a variety of chemical modifications, among which the methylation modification of the sixth nitrogen atom of RNA adenosine (N^6-methyladenosine or m^6A) has been proven as one of the most prevalent modifications [1-3]. M^6A modification occurs in one-third to one-half of all mRNA transcripts in a cell, and is particularly enriched near the stop codon or near the 5' boundary of the last exon [1,2,4]. Even in one particular cell type, there would be approximately 100,000 m^6A sites, on which the on-and-off state and quantification of m^6A methylation could be dynamically regulated in response to different conditions, as revealed by the latest high-throughput m^6A quantification method GLORI [5]. The dynamic regulatory features of the m^6A modification are closely related to the reversible enzymatic reaction system behind. On the one hand, the methyltransferase complex which consists of multiple writer proteins such as METTL3, METTL14, WTAP, ZC3H13, RBM15 and RBM15B, is able to add m^6A modification onto the RNA with the specific DRACH motifs (where D=A/G/U; R=A/G; H=A/C/U) [6]. Among them, METTL3 is able to independently methylate substrate RNA *in vitro*, and knockdown of METTL3 leads to a significant reduction of transcriptome m^6A methylation in a wide range of cells or tissues, together highlighting METTL3 as the core component of m^6A writer complex [7]. On the other hand, the m^6A modification can be removed by eraser proteins such as FTO and ALKBH5 [8]. Through sophisticated procedures executed by the m^6A writers and erasers, a complicated epitranscriptome is formed. To date, near 500,000 of single-nucleotide m^6A sites has been identified [9]. Comprehensive m^6A profiling by MeRIP-seq has revealed distinct but partly shared m^6A profiles across different cell types [10,11]. Nonetheless, considering the different transcriptome context among different cell types, direct and systematic measure of the regulatory effects of m^6A is necessary. Unfortunately, there remains a lack of sizable high-throughput profiling of m^6A's effects, and consequently, to what extent the m^6A regulatory effects are shared or distinct between different cell types is not clear.

The m^6A modification is also recognized as the top RNA modification with the greatest number of known recognizing partners, i.e. m^6A readers. This comprehensive and sophisticated reader toolkit gives rise to the diversity and complexity of the m^6A regulatory effects, i.e. m^6A readouts. Known post-transcriptional m^6A readouts includes but not limited to RNA degradation (half-life regulation),

alterations in translational efficiency and alternative splicing [7,12]. Although with controversial about functional specificity [13,14], it is recognized that several key m^{6}A readers play vital roles in gene expression regulation. For example, YTHDF1 would promote the translation of mRNAs with m^{6}A modification, while YTHDF2 would reduce the half-life of m^{6}A target transcripts [15,16]. Nuclear YTHDC1 could recruit pre-mRNA splicing factor SRSF3 and inhibit the binding of SRSF10 to mRNAs to influence exon inclusion events in alternative splicing [17]. IGF2BP family proteins constitute a new clade of m^{6}A readers that inhibit mRNA degradation and enhance translational efficiency [18]. M^{6}A participates in a wide spectrum of physiological and disease processes, where different readers contribute substantially to its regulatory mechanism [6,7]. For example, in neural development, m^{6}A methylation modification can promote mRNA degradation of JAK-STAT pathway genes by recruiting the YTHDF2 [19]. YTHDF1 can enhance the translational efficiency of genes related to Wnt/β-catenin pathway through m^{6}A-dependent manner, which ultimately promotes cancer stem cell-like activity [20]. The binding of m^{6}A modification on precursor mRNA to YTHDC1 is essential for the correct splicing of mRNAs of oocyte development-related gene [21]. Nonetheless, disruption of any one of the above m^{6}A readers cannot completely abolish even single type of regulatory effects of m^{6}A [15-18], suggesting the existence of undiscovered m^{6}A readers. Indeed, by leveraging mass spectrometry, dozens of proteins have shown favorable presence in the m^{6}A-associated proteome, although the direct m^{6}A recognition ability of these putative m^{6}A readers need further validations [22]. Until recent, novel m^{6}A readers have been unveiled. For example, ELAVL1 (HuR) preferentially binds elements in the 3'-UTR that are enriched for AU or U, thereby regulating mRNA stability [23]. TARDBP (TDP43) is identified as a m^{6}A-binding protein that regulate neurodegeneration [24].

As the key epitranscriptomic factor, m^{6}A also exert substantial impacts on key properties of pluripotent stem cells. In fact, early demonstrations of m^{6}A regulatory function on ESCs constitute the pioneer cases supporting the functional importance of m^{6}A modification. In 2014, Batista et al. reported for the first time that depletion of *Mettl3* reduced the overall level of m^{6}A modification in mouse embryonic stem cell (mESCs) and human embryonic stem cell (hESC) and facilitated the degradation of mESCs' core pluripotency transcripts including *Nanog* [25]. Geula et al. and Zhang et al. found that depletion of *Mettl3* or *Mettl14* leads to abnormal differentiation and embryonic death of mESCs [26,27]. In Induced pluripotent stem cells (iPSCs), Chen et al. also showed that increased m^{6}A

formation promotes cell reprogramming to pluripotency [28]. These results demonstrate that m^{6}A modification is essential for regulating the pluripotency state. However, there are also inconsistent results, for example, in 2014, Wang et al. found that *Mettl3* inhibition decreases the expression of pluripotency-associated genes (e.g., *Nanog* and *Sox2*) but up-regulates the expression of developmental markers (e.g., *Sox17*), and ultimately promotes mESCs differentiation [29]. In addition, Wen et al. found that perturbation of another m^{6}A writer *Zc3h13* gene impaired the self-renewal capacity of mESCs and promoted cell differentiation [30]. These results imply complexity in the functional reading-out of the m^{6}A tags in mESCs. Indeed, Lasman et al. found that neither knockdown of any of the *Ythdf* genes alone nor triple knockdown of *Ythdf1/2/3* reduced the self-renewal capacity in mESCs, whereas triple knockdown mESCs were poorly differentiated during teratoma and embryoid body formation, demonstrating the redundancy of YTHDF1/2/3 in regulating the developmental differentiation of mESCs [31]. YTHDC1 also plays an important role in the maintenance of pluripotency of mESCs and regulates the programmed cell fate during embryonic development transition through activation of genome-wide H3K9me3 histone modifications and inhibition of reverse transcriptional transposon expression [32]. As for hESCs, studies have focused on the contribution of m^{6}A writers and erasers to hESC differentiations. For example, Bertero et al. reported that SMAD2/3 can bind to the m6A methyltransferase complex, and that this binding is essential for regulating the early determination of cell fate in hESCs [33]; and overexpression of the m^{6}A demethylase ALKBH5 significantly inhibits the cardiac differentiation potential of hESCs [34]. These studies have emphasized the importance of the m^{6}A modification in regulating the self-renewal and differentiation process of hESCs. However, which and how m^{6}A readers exert the specific regulatory effects of hESC differentiation has not been sufficiently investigated.

Together, m^{6}A has emerged as the key gene expression regulatory machinery but its regulatory effects and mechanisms have not been fully elucidated. Whether m^{6}A showed similar or distinct readouts across different cell types? Are there new readers behind the regulatory effects of m^{6}A. And if so, how could these m^{6}A readers influence basic stem cell functions including self-renewal and differentiations? To this end, we comprehensively profiled the three main layers of m^{6}A readouts (mRNA half-life, translational efficiency and alternative splicing) across five common cell types of different origin (including cancerous A549 and JURKAT, and non-cancerous hESC, HEK293T and human umbilical vein endothelial cells (HUVECs)). Besides, quantitative profiling of m^{6}A

methylation by GLORI, if applicable, was also performed. To exploit these resources, machine learning modeling of the m^6A readouts was conducted, where putative m^6A readers were suggested based on the interpretation of model features. Finally, we validated a few of these putative m^6A readers and unveiled their specific impacts on hESC differentiation.

Methods

Cell culture

HEK293T and A549 cell lines were cultured in DMEM medium (Gibco, catalog#C11995500BT) supplemented with 10% fetal bovine serum (FBS, Gemini, catalog#900-108) and antibiotics. JURKAT cell line was maintained in RPMI 1640 medium (Gibco, catalog#C11875500BT) with 10% FBS (Gemini, catalog#900-108) and antibiotics. hESCs were cultivated in serum-free, defined mTeSR1 medium (STEMCELL, catalog#85850) and grown on plates coated with growth-factor-reduced Matrigel. hESCs were passaged with non-enzymatic dissociation by 0.5 mM EDTA (Beyotime, catalog#C0196-100ml). HUVECs were isolated as described [35]. The clean vein of the umbilical cord was first lavaged with 0.25% trypsin at 37°C for 15 min. HUVECs were collected and suspended in Endothelial Cell Medium (ECM, ScienCell, catalog#1001). Isolated HUVECs were cultured between passage 4–6 in ECM for experiment. Cells were grown at 37°C with 5% CO_2.

METTL3 knockdown, transfection and flow cytometry

The doxycycline-controlled Tet-Off/On gene expression systems were used for regulating the activity of METTL3 in cell lines. The sequence targeting *METTL3* were synthesized and inserted into the lentivirus vector GV307 (TetIIP-TurboRFP-MCS-Ubi-TetR-IRES-Puromycin) and the lentiviruses were purchased from GeneChem (Shanghai, China). Then according to the characteristics of different cell lines, lentiviruses transfection was performed using the HiTransG A/P developed by GeneChem. Cells transfected with shRNA lentivirus or negative control lentivirus were cultured for 48 h. The target sequence of *METTL3* was CAAGGAACAATCCATTGTT and the negative control sequence of insertion was TCTCGCTTGGGCGAGAGTAAG. Other information of the oligo synthesis was included in **Supplementary Table S1**. After the doxycycline induction for 48 h, the transfected cells

167 expressed red fluorescence (RFP) for roughly estimating the overall transfection efficiency. Cell
168 samples were resuspended in MACS buffer for fluorescence-activated cell sorting (FACS, BD
169 FACSAria™ III) to obtain high RFP expression transfected cells.

170

171 **RNA extraction**

172 Total RNA was isolated from cell samples using TRIzol (Invitrogen, catalog#15596018) following
173 the manufacturer's instruction. Briefly, cells were lysed with TRIzol reagent at room temperature
174 until the cell deposits disappear and chloroform was added. After centrifuge for 15 min at 12,000×g
175 at 4°C, the aqueous phase was transferred to the new EP tube, mixed with isopropanol and stand at
176 room temperature for 10~15 min. Then centrifuge for 10 min at 12,000×g at 4°C, the supernatant was
177 discarded and the RNA precipitate was washed with 75% ethanol. After centrifuge for 5 min at
178 7,500×g at 4°C and dry, RNA was dissolved with RNase-free water and its concentration was
179 measured by Thermo Scientific NanoDrop.

180

181 **Real-time qPCR for mRNA quantification**

182 Total RNA was extracted from transected cells scribed in 'RNA-extraction', then reverse transcribed
183 using PrimeScript RT Master Mix (TaKaRa, catalog#RR036B). All primers used for RT-qPCR were
184 listed in **Supplementary Table S2**. All RT-qPCRs were run on Bio-Rad CFX384 real-time PCR
185 detection system using PowerUp SYBR Green Master Mix (ThermoFisher Scientific,
186 catalog#A25742). GAPDH was used as internal control to normalize the data across different samples.

187

188 **Western blot**

189 Cell samples were collected, washed with ice-cold PBS and fully lysed with RIPA lysis buffer
190 containing protease inhibitors (Beyotime, catalog#P0013C) on ice. After centrifuge for 30 min at
191 12,000×g at 4°C, supernatant was collected and protein amounts were quantified using the BCA
192 Protein Assay Kit (Beyotime, catalog#P0012S). After boiling for 10 min, equal amounts of protein
193 were loaded and separated by 10% SDS-PAGE. After electrophoresis, they were transferred to PVDF
194 membranes (Merck-Millipore, catalog#ISEQ00010). Membranes were blocked with 5% non-fat milk

(Beyotime, catalog#P0216-1500g) for 1 h and then incubated at 4°C overnight with the primary antibodies. After incubating 1 h with secondary antibodies at room temperature, images were obtained using the Gel Doc EZ Imager (Bio-Rad). GAPDH was used as the loading control. All antibodies used for western blot were listed in **Supplementary Table S3**.

High-throughput profiling of m^6A readouts

Unless otherwise stated, the m^6A readouts were measured by comparing shControl (normal m^6A level) versus shMETTL3 (disrupted m^6A level) to intuitively depict the regulatory readouts in presence of m^6A. The sequencing service related to m^6A readout estimations was provided by Novogene Biotech (Tianjin, China). The experimental and computational pipelines of each readout category is described as follows:

a. mRNA half-life readout. Cells transfected with *METTL3* shRNA or negative control shRNA were re-seeded into 6 well plates. After the doxycycline induction for 48 h, actinomycin D was added to 2 μg/mL at 0 h, 1 h, 3 h and 6 h before total RNA extraction. Before construction of the library with mRNA sample, ERCC RNA spike-in control mix (Invitrogen, catalog# 4456740) was added to each sample following the manufacturer's instruction. NEBNext Ultra RNA Library Prep Kit for Illumina (NEB #E7770) and NEBNext Ultra Directional RNA Library Prep Kit for Illumina (NEB #E7760) were used with 400 ng of total RNA for the construction of sequencing libraries. ERCC spike-in were added to total RNA before library construction, following the protocol recommended by ERCC spike-in kit manufacturer. RNA libraries were prepared for sequencing using standard Illumina protocols. Two biological replicates were prepared for each time point. For each sample collected at 1 h, 3 h and 6 h, a 15G amount of paired-end sequencing reads was obtained. For 0 h sample, we required 60G amount of sequences to ensure ultra-deep RNA sequencing that is necessary for systematic alterative splicing assay. This differences in data size were properly controlled by the aforementioned ERCC spike-ins. More specifically, quality control, adapter cutting and low-quality sequence removal were performed by FastQC, fastp and FASTX toolkits. The clean reads were mapped to human genome (hg38) by HISAT2 software (v2.2.1) and the expression values were calculated by featureCounts command of RSubread package with suggested parameter of the software. The absolute quantification of each sample was performed by using ERCC RNA spike-ins as the reference,

following Wang et al. [15]. The mRNA half-life was also estimated following the method modified from [15]. The degradation rate of RNA k was estimated by:

$$\log_2(A_t/A_0 \cdot \delta) = -kt$$

where t is transcription inhibition time (h), A_t and A_0 represent mRNA quantity at time t and time 0, δ is a regulating factor in case the RNA:ERCC ratio is prominently deviated from the expectation. k values of 3 h and 6 h were calculated: time 3 h versus time 0 h, and time 6 h versus time 0 h. A 1.5-fold change of half-life threshold was applied for subsequent analysis.

b. translational efficiency readout. The translational efficiency was measured by ribosome profiling sequencing (Ribo-seq). The reported protocols [36] was adapted with the following modifications: Before cells collection, cycloheximide (CHX, HARVEYBIO, catalog#C21865-100mg) was added to the culture media at 100 μg/mL for 5 min. Eighty million cells from each group were collected, rinsed in ice-cold PBS with 100 μg/mL CHX. After centrifuge for 5 min at 500×g at 4°C, cells were resuspended in cell freezing medium with 100 μg/mL CHX for dry ice transportation. Two replicates were prepared and the reads were processed and analyzed with the similar pipeline to the above part a. To comply with the Ribo-seq convention, the R1 reads were used for subsequent analysis. The Xtail software (v1.1.5) was utilized to measure the changes of translational efficiency with default parameter [37]. To ensure sufficient number of genes for subsequent analysis, a relaxed thresholds of 1.5-fold change and $P < 0.05$ were applied. We also considered public Ribo-seq data from GEO database for the machine learning modeling described later, including those from HeLa (GSE117299), HepG2 (GSE121952), Huh7 (GSE155447) and MOLM13 (GSE98623). These data were analyzed with the same pipeline.

c. alternative splicing readout. We exploited the ultra-deep sequencing of 0 h samples as described in the above part a to measure alternative splicing events. Two replicates were prepared and the reads were processed and analyzed with the similar pipeline to the above part a. The alternative splicing events and exon inclusion ratio (Psi) were calculated by rMATS-turbo (v4.1.0, default parameter) [38]. A change of exon inclusion ratio (delta-Psi) no less than 0.1, together with FDR < 0.05, were selected as the significant alternative splicing event.

d. Functional analysis. The functional enrichment of Gene Ontology (GO), Kyoto Encyclopedia of Genes and Genomes (KEGG), WikiPathways and MSigDB functional gene sets were performed by

253 ClusterProfiler with default parameter and cutoffs [39]. Gene dependency score was obtained from
254 DepMap database [40].

255 **High-throughput profiling of m^{6}A methylation sites**

256 ***a. GLORI sequencing.*** Recently, Liu et al. developed GLORI, an antibody-independent sequencing
257 technique for single-base quantitative detection of m^{6}A methylation [5]. The main idea of GLORI is to
258 find a catalytic system of glyoxal and nitrite through chemical reaction combination screening, which
259 efficiently deaminate unmethylated adenosines to inosines (A-to-I), but not methylated ones. We
260 used this state-of-the-arts technique for the quantitative profiling of m^{6}A methylation in A549, hESC
261 and JURKAT. The GLORI-identified m^{6}A sites in HEK293T was directly obtained from the original
262 study [5]. HUVEC was not included because of the required large amount of input cells by GLORI
263 sequencing service. GLORI sequencing service was provided by Cloud-Seq Biotech (Shanghai,
264 China). Total RNA from the samples was extracted using TRIzol, and RNA was purified according
265 to the MEGA clear transcription purification kit (Thremo fisher, catalog#AM1908). RNA was
266 incubated with fragmentation buffer (NEB, catalog#E6150S) for 4 min at 94°C and glyoxal solution
267 and DMSO were added, and the mixture was incubated for 30 min at 50°C in a preheated thermal
268 cycler. minutes, and at the end of the incubation, the tubes were brought to room temperature, and
269 then saturated H_3BO_3 (Sigma-Aldrich, catalog#B0394) solution was added. The incubation was
270 continued at 50 °C for 30 min, and was then added to the pre-configured deamination buffer (750
271 mM $NaNO_2$ (Sigma-Aldrich, 31443), 40 mM MES (pH 6.0), and 10 μL of glyoxal solution for a total
272 of 8 h of incubation. Finally, RNA was purified by ethanol precipitation, and sequencing libraries
273 were constructed by GenSeq Low Input RNA Library Prep Kit (GenSeq, Inc.) following the process
274 of the instructions provided by the manufacturer. The constructed sequencing libraries were subjected
275 to quality control and quantification by BioAnalyzer 2100 system (Agilent Technologies, USA),
276 followed by 150 bp paired-end sequencing.

277 ***b. GLORI data analysis.*** Quality control of raw reads was first performed using Q30. Then cutadapt
278 software (v1.9.3) was used for read de-multiplex and removal of low-quality reads. PCR duplicates
279 were removed based on Unique Molecular Identifiers (UMI) tags. Clean reads were aligned to the
280 reference genome (hg38) and BAM files were obtained using STAR (v2.7) and bowtie2 (v2.2.4)
281 software. To ensure acceptable m^{6}A site detection rate, we performed two rounds of sequencing, and
282 the aligned BAM files from these two rounds were combined by samtools (v1.12). Finally, the m^{6}A

sites were called and quantified by GLORI-tools [5] with parameter "--combine --rvs_fa -c 1 -C 0 -r 0.1 -p 0.05 -adp 0.05". Finally, only m^6A sites that showed modification rate > 0.1 for both replicates were retained [5].

c. Public MeRIP-seq methylation profiles. Currently, GLORI methylation profiles are not available for most cell lines. To obtain m^6A sites for other cell types, we exploited widely used MeRIP-seq-based m^6A methylation profiles [1,2]. To ensure comparable results, raw sequences of MeRIP-seq studies were obtained from GEO (as specified in **Supplementary Table S4**). The adapter trimming and quality control was performed by fastp, and the reads were aligned to human genome (hg38) by HISAT2. Finally, exomePeak2 was used to call m^6A peaks [9,41]. To obtain single-nucleotide m6A sites, we compared m6A peaks with known single nucleotide m^6A sites from m6A-Atlas V2.0 database [9] and GLORI technique by using bedtools (v2.31.0). Sites following the consensus m^6A motif DRACH were retained.

Machine learning modeling of readouts

a. Obtaining RNA binding protein (RBP) binding site annotations: Our m^6A readout prediction models were heavily relied on transcriptome-wide annotation of RBP binding sites. CLIP-seq and its derivates constitute the major source of such annotation. We obtained CLIP-seq (and derivates)-based RBP binding sites from POSTAR2 database [42]. We did not consider POSTAR3 because there was no RBP binding site score in the downloadable data of POSTAR3. Moreover, to make our annotations up-to-date, we obtained and re-analyzed raw CLIP-seq data from GEO, and adopted a pipeline similar to that of POSTAR database to process these data. Briefly, raw reads were filtered and trimmed by fastp and cutadpat software, and aligned to human genome (hg38) by using bowtie (v1.3.0, for short reads) or STAR (for longer reads). Samtools was used to process the aligned reads and the RBP binding regions were called by Piranha (v1.2.1) with recommended parameters [43]. We also obtained eCLIP-based annotation from ENCODE projects [44]. We noted that the default merging of biological replicates in ENCODE would result in very limited binding sites for some RBPs. To this end, we also used bedtools to obtain the union of RBP binding regions derived from both replicates to enhance the sensitivity and transcriptome coverage. Finally, RBP site annotations from non-CLIP techniques were directly obtained from the corresponding GEO accession. The summary of RBP binding site profiles were available in **Supplementary Table S5**.

b. Feature encoding and model training: For predicting half-life and translational efficiency readouts, eleven set of features were considered: 1) The score of RBP binding site with the nearest distance on the genome; 2) The score of RBP binding site with the nearest distance on the transcripts; 3) The minimum RBP-to-m^6A-site distance among different m^6A sites of the same gene on the genome; 4) The minimum RBP-to-m^6A-site distance on the transcripts; 5) The maximum RBP-to-m^6A-site distance on the genome; 6) The maximum RBP-to-m^6A-site distance on the transcripts; 7) The site to gene topology (e.g. minimum distance to start codon); 8) Tissue expression level, as measured by GTEx project [45]; 9) Gene dependency score, as record by DepMap database [40]; 10) Nearest distance to a 6-mer on transcript; 11) Maximum counts of a specific k-mer in ±100 nt range flanking known m^6A sites. As for the prediction of exon inclusion ratio alterations, we used the annotation of the closest m^6A site to the exon boundary to encode features (if any within 10kb of exon boundary). Since only one representative m^6A site was considered for each exon, no minimum/maximum operation of RBP features among multiple m6A sites on the same gene was required. Besides, as an exon-level prediction, gene features like GTEx tissue expression and DepMap gene dependency score were also not included.

c. Machine learning model: We exploited XGBoost [46] to model the readouts for each readout and each cell type. XGBoost has been successfully implemented in both bioinformatic prediction and clinical application [47,48]. Ten-fold cross-validation to train and test the model, and the overall performance was measure by receiver operating characteristic (ROC) curve and area under ROC curve (AUC). A heustic search of best combination of feature set was performed to measure the AUC gain of the feature set. And for RBP features, the feature importance score derived from the XGBoost models.

RNA pull-down

The RNA oligonucleotides [ss-A: 5'-CGUCUCGGACUCGGACUGCU-3'; ss-m^6A: 5'-CGUCUCGG(m^6A)CUCGG(m^6A)CUGCU-3'] with the same sequences of ss-A and ss-m^6A were synthesized by Rui Biotech (Beijing, China). RNA pull-down assay was conducted by the Pierce™ Magnetic RNA-Protein Pull-Down Kit (Thermo Fisher Scientific, catalog#20164). The included Thermo Scientific Pierce RNA 3' Desthiobiotinylation Kit (catalog#20163) was used to label the target RNA. Next, biotin-labeled RNA oligonucleotides containing adenosine or m^6A (50 pmol) were

343 immobilized onto 50 μL streptavidin magnetic beads in binding buffer at room temperature for 15-
344 30 min. RNA-conjugated streptavidin beads were then incubated with 200 μg total proteins from
345 target cells in binding buffer in a final volume of 100 μL at 4°C for 30-60 min. RNA-protein complex-
346 containing beads were washed three times with wash buffer. After extensive washing, RNA-binding
347 protein complexes were boiled and eluted in 1 × SDS loading buffer to separate on 10% SDS-PAGE
348 gels for western blot analysis.

349

350 **RBP binding site profiling by HyperTRIBE**

351 ***a. HyperTRIBE plasmids construction and transfection.*** HyperTRIBE is a promising high-
352 throughput sequencing technique for identifying potential binding site of an RBP. Leveraging
353 plasmid fusing target RBP with hyperactive ADAR, the RNA editing signals close to the RBP binding
354 site can be detected at transcriptome level through conventional RNA sequencing [49]. Here, the
355 hyperactive ADAR containing TRIBE plasmids were constructed by Rui Biotech (Beijing, China).
356 The control plasmid, mammalian expression plasmid, containing mCherry ADAR control and p2A
357 GFP reporter can be obtained from Addgene (Plasmid #154786). As for RBP-TRIBE plasmid, using
358 standard restriction enzyme-based cloning to clone known and putative m^6A reader RBPs (YTHDF1,
359 DDX6, FUBP3, FXR2 and L1TD1) into TRIBE plasmid. Sanger sequencing was used to confirm
360 proper insertion and then control and RBP-ADAR plasmids were infected into hESCs by transfection
361 reagent jetOPTIMUS (Polyplus, catalog#101000051). After transient transfection into target cells for
362 24 h, the cells containing RBP-ADAR fusion or ADAR alone proteins were sorted by GFP and
363 mCherry fluorescence and using TRIzol reagent to extract the total mRNA from the sorted cells.

364 ***b. TRIBE sequencing and analysis.*** RNA-sequencing for cells transfected with HyperTRIBE
365 plasmid were conducted by Novogene Biotech (Tianjin, China). Messenger RNA was purified from
366 total RNA using poly-T oligo-attached magnetic beads. After fragmentation, the first strand cDNA
367 was synthesized using random hexamer primers followed by the second strand cDNA synthesis. After
368 library quality control, quantified libraries were pooled and sequenced on Illumina NovaSeq with
369 paired-end 150-bp reads, providing sequencing data at 40G per library. According to Biswas et al.'s
370 protocol [50], firstly, cutadapt was used to remove the adaptor and low-quality reads. Clean reads were
371 then aligned to the reference genome (hg38) by using STAR software. Picard (v3.3.0) was used to
372 remove duplicates and sort the output BAM files. To identify editing sites, we used Bullseye, a set of

373 Perl scripts which was originally developed by Flamand et al. for analysis of editing events induced
374 by transfected plasmids [13]. BAM files were parsed to generate coverage matrices at each position in
375 the genome, excluding duplicate and multi-mapped reads. Editing sites for HyperTRIBE in individual
376 samples were then called by comparing A2I mutation rates at all positions within annotated exons
377 (hg38) with samples expressing ADAR alone. Sites edited at rates between 5% and 99%, edited to
378 higher levels than control cells (1.5 × for A2I), with at least two mutations, and that did not overlap
379 annotated SNP were kept for further analysis. The final list of sites was identified as those found in
380 three replicates and with an average editing rate of at least 5% in all samples where sites were called.
381 To identify the binding motif of the editing sites, we broadened each site by 500 bp in each direction
382 and then imported into HOMER software [51] for *de novo* motif identification. It is worth mentioning
383 that because we are interested in identification of m^6A-binding proteins, we further focused on the
384 proteins that have motifs containing 'RRACH', which represents the most common m6A consensus
385 sequence. To investigate the binding preference of the RBPs near m6A sites, BAM alignments were
386 further processed using deepTools [52]. Heatmaps and profiles were generated using the plotHeatmap
387 and plotProfile script from the deepTools suite.

388

389 **CRISPR-mediated *FUBP3*, *FXR2* and *L1TD1* knock out (KO)**

390 The CRISPR-Cas9 knock-out vector, containing cassettes for GFP, Cas9 endonuclease, and the
391 double guide RNA (gRNA) moiety designed to target FUBP3, FXR2 and L1TD1, was custom
392 synthesized by Guangzhou Regenverse Therapeutics Co., Ltd. (Guangzhou, China). After plasmid
393 transfection for 48 h, GFP+ hESCs were sorted using flow cytometry, and plated at low density for
394 single-colony isolation. Selected single colonies were tested by western blot for loss of protein.
395 Mutations were validated by sequencing products of PCR amplification of the regions flanking the
396 targeting sites.

397

398 **Cell proliferation assays**

399 ***a. Cell counting kit 8 (CCK8) assay.*** Human embryonic stem cells (hESCs) were digested into single
400 cell suspension using Accutase (Merck-Millipore, catalog#SCR005) and the number of cells were
401 counted by automated cell counter (RWD, catalog#C100). After counting, the cells were seeded in

402 Matrigel-coated 96-well with a cell density of 2000 cells per well. After appropriate cultivate time,
403 10% CCK8 (Dojindo, catalog#CK04) was added into the culture medium and incubate cells for 2 h,
404 then optical density value at 450 nm was detected using a microplate reader. Cells were detected in
405 every 24 h.

406 ***b. Alkaline phosphatase staining assay.*** For ALP (alkaline phosphatase) staining, hESCs were
407 digested into single cell suspension using Accutase and the number of cells were counted by
408 automated cell counter. After counting, the cells were seeded in Matirgel-coated 12-well with the cell
409 density of 1.2×10^5 cells per well and incubated in mTeSR1 medium for 3 days. Then the cells were
410 fixed with 4% paraformaldehyde for 3–5 min followed by washing with PBS. Next, the samples were
411 added with BCIP/NBT staining solution (Beyotime, catalog#C3206) for 15 min in dark at room
412 temperature. The usage of regents was followed with the manufacturer's recommendations. The cell
413 images were taken after washing the cells with PBS.

414

415 **hESCs differentiation assays**

416 ***a. Endodermal differentiation.*** To initiate endodermal cell differentiation, hESCs were cultured on
417 Matrigel-coated 6-well plate in RPMI1640 basal medium supplemented with B27 (Gibco,
418 catalog#12587-010) and 100 ng/ml Activin A (Peprotech, catalog#AF-120-14E-10UG). After cell
419 differentiation inducing for 3 days, endoderm markers were detected by flow cytometry and RT-
420 qPCR analysis.

421 ***b. Hematopoietic mesodermal differentiation.*** For Hematopoietic mesodermal differentiation,
422 hESCs were cultured to 60% density on Matrigel-coated plates. Using Accutase to digest cells for 3-
423 5 min, the cells were resuspended by blowing with mTeSR1 and seeded into ultra-low attachment 6-
424 well plates with the cell density of 2×10^5 cells per well. Cells were cultured in a hypoxic incubator
425 (5% CO_2, 5% O_2) for 24 h, until they formed to embryoid bodies (EB). To induce mesodermal
426 differentiation, STEMdiff APELTM2 (STEMCELL, catalog#05270) was used as the basal medium,
427 and the differentiation medium was configured by adding corresponding cell factors according to the
428 Kaufman hematopoietic differentiation protocol [53]. After cell differentiation inducing for 6 days,
429 mesodermal markers were detected by flow cytometry and RT-qPCR analysis.

430 ***c. Neural ectodermal differentiation.*** Monolayer culture protocol was used to initiate neural
431 ectodermal differentiation. hESCs were plated onto Matrigel-coated 6-well plates with the cell
432 density of 2×10^5 cells/cm^2, and then cultured in STEMdiff Neural Induction Medium (STEMCELL,
433 catalog#08581) added with SMADi. After cell differentiation inducing for 3 days, neural ectodermal
434 markers were detected by flow cytometry and RT-qPCR analysis.

435

436 **Statistical analysis**

437 Unless otherwise stated, bar charts represent the mean ± standard deviation of the mean (SD), and
438 the results for the two groups were compared using a two-tailed unpaired Student's *t*-test. A *P*-value
439 smaller than 0.05 was considered significant unless stated differently, and the exact degree of
440 significance as indicated by asterisks is stated in the legends. Statistical significance was presented
441 as $*P < 0.05$, $**P < 0.01$, $***P < 0.001$ and $****P < 0.0001$; ns indicates $P > 0.05$.

442

443 # Results

444 **Systematic profiling of m^{6}A methylation readouts across different cell types**

445 M^{6}A targets a wide spectrum of pathways in cells, but how does its regulatory effects overlap between
446 different cell types has not been comprehensively investigated. To this end, we systematically
447 profiled three main m^{6}A readouts (i.e. mRNA half-life, translational efficiency and alternative
448 splicing) by utilizing m^{6}A-disrupted cells and various high-throughput sequencing techniques. The
449 overall design of this study is illustrated in **Figure 1A**. Briefly, we perturbed m^{6}A in five
450 representative cell lines (A549, hESC, HEK293T, JURKAT and HUVEC) through knockdown of
451 core component of m^{6}A methyltransferase complex METLL3 [7]. The efficiency of the knockdown
452 was verified by qRT-PCR and Western blot, as shown in **Supplementary Figure S1**. By procedure,
453 we could measure the readouts of m^{6}A by comparing the post-transcriptional gene expression
454 dynamics between m^{6}A-normal cells (i.e. shControl cells) and m^{6}A-disrpted cells (i.e. shMETTL3
455 cells). Actinomycin D-treated temporal RNA-seq (15G per sample), Ribo-seq and ultra-deep RNA-
456 seq (60G per sample) were adopted to measure the three main categories of m^{6}A readouts,
457 respectively. Because three high-throughput experiment designs share an untreated/input group, we

introduced a cost-effective experiment design by performing ultra-deep RNA-seq on the untreated (0h) cells, which could also serve as the start point for temporal RNA-seq as well as the input sample for Ribo-seq. Samples at 1h, 3h and 6h after transcription inhibition by actinomycin D was collected and submitted to RNA-seq, and the mRNA half-life was measured by fitting the gene expression to the mRNA decay curve along the time points. It is noteworthy that we have introduced ERCC RNA spike-in in proportion to the input RNA samples, and calculated the absolute gene quantification based on the ERCC spike-in counts, thereby cancelled the discrepancy in sequencing library size between 0h time point and others (see Methods). For all cell types, a decrease of absolute mRNA quantification along the time points were observed, demonstrating substantial mRNA degradation with the transcription process inhibited. Nonetheless, the decay rate of the mRNA half-life could be diverged between different m^6A states, where for most of the cell types, an overall down-regulation of mRNA half-lives in m^6A normal cells (shControl cells) could be observed (**Figure 1B**), which is consistent with the function of METTL3 in promoting mRNA degradation as previously reported in the literature [15,19]. Nonetheless, the overlap of half-life down-regulated genes is limited between different cell types, indicating a high cell-type specificity of the half-life readout of m^6A (**Figure 1C**). It is possible that the limited overlap between down-regulated genes is simply caused by the threshold in measuring the readout. Thus, we performed enrichment for different functional gene sets and pathways to check if different cell types could show consistent changes at the pathway level. Indeed, gene sets representing fundamental biological functions such as mitochondrial oxidative phosphorylation, glycolysis and DNA repairs were shared by multiple cell types, indicating a consensus regulation by m^6A in these basic cellular functions (**Figure 1D-E**). On the other hand, some pathways were only enriched in particular cell type, and these pathways are likely to be associated the functions of specific cell type. For example, multiple oncogenic pathways were enriched in lung cancer cell line A549, whereas cytoskeletal and endothelial cell migration functions were enriched in blood vessel-derived HUVEC cells (**Figure 1F-G**).

By querying to the public MeRIP-seq methylation profiles from the corresponding cell type, we confirmed that most (>90%) of the half-life down-regulated genes were the direct target genes of m^6A methylation (**Figure 1H**). To precisely describe the relationship between m^6A modification levels and half-life changes, we evaluated the m^6A methylation levels of target genes in different cells using GLORI, a state-of-the-art absolute quantification technology for m^6A methylation [5]. The

quantitative m^6A map of four out of the five cell types were included, where A549, hESC and JURKAT data were newly measured in this study, while HEK293T data was obtained from the original literature [5]. HUVEC was not included in GLORI analysis because of its proliferation capacity is insufficient to accumulate required amount of input cells. The m^6A methylation sites identified by GLORI were all enriched near the stop codon (**Supplementary Figure S2A**), which is a typical topology feature of m^6A sites on coding genes [2]. Compared with the original GLORI results, our GLORI experiments show relative underrepresentation of m^6A sites with low modification ratios, partly because of the reduced sequencing depth in this study due to the cost concerns (**Supplementary Figure S2B**). Nonetheless, an observable fraction of m^6A sites were shared between different cell types, and the overlap was even more prominent at the gene level (**Supplementary Figure S2C-D**). Besides, a noticeable overlap between m^6A target genes identified by GLORI and those from MeRIP-seq could be observed (**Supplementary Figure S2E**). Finally, >80% of the half-life down-regulated genes harbored a GLORI-derived m^6A site (**Supplementary Figure S2F**), which not only supported the representativeness of GLORI-based methylation profile but also enabled a direct correlation analysis between the absolute quantification of m^6A sites and the mRNA half-life fold-change of their target genes. The results showed that there were significant correlations between m^6A modification rates and the half-life changes in most cell, suggesting the half-life regulation would partly rely on the methylation level of the target genes. Nonetheless, the correlations were generally weak (**Figure 1I**), suggesting that other factors, such as the genomic context of the m^6A methylation site, may have a significant impact on the functional readout of m^6A.

Next, we profiled the translational efficiency readout of m^6A by comparing the translational efficiency of m^6A-normal cells versus those of m^6A-disrupted cells. In terms of translational efficiency, different cell types showed more balanced changes, with roughly comparable numbers of up- and down-regulated genes (**Figure 2A**). The overlap of genes showing translational efficiency changes was also very limited between different cell types, for both up- and down-regulated genes (**Figure 2B-C**). Some of the genes showed both half-life and translational efficiency changes, and this tendency was particularly evident in JURKAT (**Figure 2D and Supplementary Figure S3A-C**). In A549 cell lines, genes with half-life or translational efficiency changes had higher importance (as measured by DepMap cancer cell line gene dependency score [40]) than background and those with both types of changes ranked the highest (**Figure 2E**). In JURKAT, a higher importance of m6A-

regulated genes was also observed, but genes with both types of changes did not show significantly higher importance, partly because of higher overlap between two groups of genes in JURKAT (**Figure 2D**). Similar to the observation in half-life readout analysis, some fundamental pathways are also the favored target of the translational efficiency regulations of m^6A (**Supplementary Figure S3D-I).** Finally, more than 90% of translational efficiency-change genes were also the m^6A methylation target genes, as suggested by the MeRIP-seq methylation profiles (**Figure 2F**). When considering GLORI-based methylation profiles, approximately 80% of genes showing translational efficiency changes could be targeted by m^6A (**Supplementary Figure S2G**). However, GLORI-estimated methylation levels were only weakly correlated or non-significantly correlated with the fold change in translational efficiency (**Figure 2G**). We also noted that genes with up- or down-regulated translational efficiency did not always tend to have a m^6A site near the start codon (**Figure 2H**). These results indicate that neither m^6A level nor m^6A topology is sufficient to fully explain the translational efficiency readout of m^6A.

The ultra-deep sequencing of 0h samples also enabled extensive detection of alternative splicing events. The results suggest that m^6A-mediated alternative splicing was mainly manifested as exon skipping, at both the event and the gene level (**Figure 3A**). Therefore, subsequent analyses of alternative splicing were focused on exon skipping. Generally, an increase of exon inclusion rate could be observed in m^6A-normal cells (**Figure 3B**), consistent with the previous study [17,21]. Genes showed altered exon exclusion ratio (Psi) were less shared between different cell types for both down- and up-regulated ones (**Figure 3C-D**). Basic functions like organelle organization and DNA repair are enriched for these genes (**Supplementary Figure S4**). However, it is noteworthy that only a small proportion of these exons had known m^6A methylation sites in their vicinity, suggesting that there might be a greater influence of indirect factors on the observed exon inclusion changes (**Figure 3E and Supplementary Figure S2H**). To reduce the influence of indirect factors, for the subsequent analysis we only considered exons with m^6A methylation sites within 10kb flanking the exon boundary. For these exons, the distance from the m^6A methylation site to the exon boundary was only weakly or not significantly correlated with the exon inclusion ratio (**Figure 3F**). In addition, GLORI-estimated methylation levels were only weakly correlated or not significantly correlated with changes in exon inclusion ratio (**Figure 3G**), suggesting that simple transcript topological features are not sufficient to predict the functional alternative splicing readout of m^6A.

551

552 **Predicting m^{6}A readouts based on the RBP binding context**

553 Given that m^{6}A methylation level and topology could not accurately predict m^{6}A functional readout,
554 we paid more attention on the genomic context, especially the RBP binding context of the m^{6}A sites.
555 To this end, we systematically collected and re-analyzed high-throughput RBP binding site data from
556 public databases (including but not limited to PAR-CLIP-seq, iCLIP-seq, eCLIP-seq, PIE-seq,
557 TRIBE, etc.; **Supplementary Table S5**) to construct the comprehensive association characteristics
558 between m^{6}A methylation sites and RBP binding sites. To ensure applicability, we used MeRIP-seq-
559 based m^{6}A site annotation of each cell type (see Methods; **Supplementary Table S4**). The score of
560 the closest RBP binding site and the genomic/transcript distance were calculated as the RBP feature
561 of an m^{6}A site. We also introduced the distribution features of m^{6}A sites in transcripts, tissue
562 expression level, gene importance score and k-mer features to better characterize m^{6}A sites and their
563 target genes. The above features were inputted into the XGBoost model to build the m^{6}A functional
564 readout predictor, hereafter referred as Reading-m6A. Reading-m6A could deal with five functional
565 readout categories: half-life down-regulation, translational efficiency down-regulation and up-
566 regulation, and exon inclusion ratio decrease or increase. The half-life up-regulation cases were not
567 considered due to the small number of this type of genes. Because of the obvious differences in m^{6}A
568 readout between different cells, each cell type was modeled separately and the prediction accuracy
569 of the model was assessed using a ten-fold cross-validation. The results showed that the overall
570 prediction performance of the model was acceptable, with an average AUROC of 0.8, especially for
571 half-life and alternative splicing functional reads (**Figure 4A-E**). To test the applicability of this
572 modeling approach, we also introduced translational efficiency readout data derived from public
573 Ribo-seq data. Four cell lines (HeLa, HepG2, Huh7 and MOLM13) were included in the translational
574 efficiency predictor. The results show that the predictive performance of the model is equally
575 acceptable in other cell types except MOLM13 (**Fig. 4B, C**). Compared to other classical machine
576 learning frameworks, XGBoost showed the best performance for most cases (**Supplementary Figure**
577 **S5A**); and its performance is insensitive to hyperparameter optimization, with at most 0.01 AUC gain
578 after hyperparameter optimization (**Supplementary Figure S5B**). We also checked whether
579 considering GLORI-based m^{6}A sites, especially their m^{6}A modification rates, could result in better
580 prediction performance. The results demonstrated that replacing MeRIP-seq-based m^{6}A site

annotation with GLORI-based ones could benefit the performance in some cases but reduce the performance in other cases, even the highly extensive GLORI profile from HEK293T was adopted, while including m^{6}A modification rate features show marginal influence to the performance (**Supplementary Figure S5C**). Therefore, we kept MeRIP-seq-based m^{6}A site annotation as the primary source to build our models.

One of the main reasons we used the XGBoost framework for modeling was its good interpretability of the model. We found that the RBP-based feature sets indeed ranked the best for their contribution to AUC. For half-life and translational efficiency readout predictions, the binding scores of RBP-binding sites near the m^{6}A site were the most important feature set (**Figure 4F-G** and **Supplementary Figure S5D**). While the transcript of genomic distance between m^{6}A and RBP-binding site ranked top in exon inclusion readout predictions (**Supplementary Figure S5E-F**). Gene topology features and tissue expression could also contribute to the performance to a much smaller extent. K-mer features showed only marginal or no contribution to AUC, implying the context features related to m^{6}A readouts were largely covered by currently known RBP binding sites. Moreover, further analysis of the importance scores of individual RBP features revealed that some known m^{6}A readers had high importance scores, while other important RBP features suggested putative novel m^{6}A readers, for which we will be experimentally validated in the next sections (**Figure 4H**).

M^{6}A readout-related RBPs as the novel m^{6}A readers

We noticed some RBPs with high feature importance in our m^{6}A readout models have been reported as m^{6}A readers [7]. These RBPs included classical m^{6}A readers such as YTHDF1/2/3, YTHDC1/2 and IGF2BPs as well as some recently discovered m^{6}A readers like TARDBP and ELAVL1 (**Figure 4H**). To further screened novel m^{6}A-binding proteins, we used methylated single-stranded RNA bait (ss-m^{6}A, with the consensus sequence GG(m^{6}A)CU) or unmethylated control RNA (ss-A) for RNA pull-down assay followed by western blot in A549 and hESC cells , where several known m^{6}A readers (YTHDF1, YTHDC2, RBFOX2, TARDBP) were included as the positive controls (**Figure 5A-B** and **Supplementary Figure S6**). The pull-down screening was mainly performed in A549 cells, and the results showed that DDX6, FUBP3 and FXR2 could strongly bind to the methylated bait (ss-m^{6}A)

instead of the unmethylated control (ss-A) (**Figure 5A**), and their binding to m^6A was also confirmed in hESCs (**Figure 5B**). Because L1TD1 has no expression in A549 cells, we could only validate L1TD1 binding to methylated bait (ss-m6A) in hESCs only (**Figure 5B**).

We further investigated the transcriptome-wide binding preference of these RBPs toward m6A sites by using TRIBE/HyperTRIBE technique for transcriptome-wide mapping of the RNA targets of RBPs [49,54,55]. TRIBE involves fusing the target RBP to the catalytic domain of the RNA editing enzyme ADAR. When the fusion proteins are expressed in target cells, the A-to-I editing at residues in proximity to RBP binding sites was catalyzed by ADAR, providing a signal detectable in conventional RNA-seq (**Figure 5C**). HyperTRIBE exploits a mutated version of ADAR domain to improve its activity thus enhance the A-to-I signals [49,55]. To demonstrate the feasibility of HyperTRIBE approach, we firstly applied this technique to well-known m^6A reader YTHDF1 in HEK293T cells. Wild-type HEK293T cells were transfected with plasmids expressing the mutated human ADAR2 catalytic domain (ADARcd-E488Q), resulting in cells expressing YTHDF1-ADAR fusion proteins which were the positive control (**Figure 5D**). Cells transfected with plasmids expressing mCherry-ADAR fusion proteins were used as the negative control. After applying stringent thresholds and subtracting negative control sites and sites with known genetic variation similar to A-to-I (see Methods) than 100,000 sites targeted by YTHDF1-ADAR fusion protein were observed. *De novo* motif analysis revealed that YTHDF1 significantly bind to the GGACU consensus sequence, which is a sub-motif of the DRACH m^6A consensus motif (**Supplementary Figure S7A**). Furthermore, over 90% YTHDF1 target genes significantly overlapped with known m^6A-modified genes identified by GLORI ($P < 1.0e-200$, Fisher's exact test; **Supplementary Figure S7B**). Additionally, we found that the majority of YTHDF1 target genes found by HyperTRIBE were overlapped with the YTHDF1 target genes identified by the previous TRIBE assay from Flamand et al. [13] (**Supplementary Figure S7C**), and with known m^6A target genes from MeRIP-seq assay [25] (**Supplementary Figure S7D**). These results together demonstrate the feasibility of HyperTRIBE.

Then we applied HyperTRIBE to DDX6, FUBP3, FXR2 and L1TD1 proteins in hESCs. We transfected plasmids expressing the fusion proteins of ADAR and candidate m^6A reader (DDX6, FUBP3, FXR2 or L1TD1) in wild-type hESCs. The enrichment heatmaps and profiles showed that

641 DDX6, FUBP3, FXR2 and L1TD1-binding sites were all notably enriched near m^{6}A sites rather than
642 non-m^{6}A sites (**Figure 5E**). The *de novo* motif analysis revealed that DDX6, FUBP3, FXR2 and
643 L1TD1-binding regions significantly enriched for the DRACH m^{6}A consensus motif (**Figure 5F**).
644 When comparing DDX6, FUBP3, FXR2 and L1TD1 target genes with the m^{6}A target genes identified
645 either by our GLORI profiling or by MeRIP-seq [25], noticeable overlaps could be observed (**Figure**
646 **5G** and **Supplementary Figure S7E-H**). Taken together, these results demonstrated that DDX6,
647 FUBP3, FXR2 and L1TD1 are novel m^{6}A readers in hESCs.

648

649 **Effect of m^{6}A readers on early differentiation in hESCs**

650 The regulatory function of DDX6 in hESCs has been clarified [56], but the functions of FUBP3, FXR2
651 and L1TD1 in hESCs have not been fully elucidated. To investigate potential roles for FUBP3, FXR2
652 and L1TD1 in self-renewal and early differentiation of hESCs, we constructed *FUBP3*, *FXR2* and
653 *L1TD1* knockout (KO) hESCs by using the CRISPR/Cas9 gene-editing approach. Western blot assay
654 showed that *FUBP3*, *FXR2* and *L1TD1* KO hESCs were successfully established (**Supplementary**
655 **Figure S8A**). Sanger sequencing of genomic DNA identified that all corresponding gene-deficient
656 clones carried the expected deletion (**Supplementary Figure S8B**). There were no significant
657 differences in cell morphology between *FUBP3*, *FXR2* and *L1TD1* KO hESCs and wild-type hESCs
658 (**Figure 6A**). Western blot was used to detect the protein level of core pluripotent markers OCT4,
659 SOX2 and NANOG in *FUBP3*, *FXR2*, *L1TD1* KO and wild-type hESCs. Compared to wild-type
660 hESCs, the expressions of OCT4, SOX2 and NANOG did not have significant changes in FUBP3,
661 FXR2 and L1TD1 KO cells (**Supplementary Figure S9A-B**). RT-qPCR analysis revealed that the
662 mRNA expression levels of OCT4, SOX2 and NANOG had no significantly differences between
663 FUBP3, FXR2 and L1TD1 KO hESCs and wild-type hESCs (**Supplementary Figure S9C**). These
664 results revealed that FUBP3, FXR2 and L1TD1 had no significant impact on the expression of core
665 pluripotent genes in hESCs. Next, we employed the CCK8 and ALP staining assays to investigate
666 the effects of FUBP3, FXR2 and L1TD1 on stem cell proliferation. CCK8 assay showed that the
667 growth rate of *L1TD1* KO cells was significantly higher than that of wild-type hESCs at 24 h, and
668 the growth rate of *FXR2* KO cells was significantly lower than that of wild-type hESCs at 48 h, but
669 there was no significant difference in proliferation rate between *FUBP3*, *FXR2* and *L1TD1* KO
670 hESCs and wild-type hESCs at 72-120 h after cell inoculation (**Figure 6B**). The ALP staining assay

showed no obvious distinction was found in the number of colonies formed by *FUBP3*, *FXR2* and *L1TD1* KO hESCs in comparison with wild-type hESCs (**Figure 6C** and **Supplementary Figure S9D**), indicating that deletion of FUBP3, FXR2 and L1TD1 had no significant effect on the proliferation rate of hESCs. Overall, these results indicated that m^6A readers FUBP3, FXR2 and L1TD1 had no prominent impact on self-renewal of hESCs.

Next, we investigated the effect of m^6A readers FUBP3, FXR2 and L1TD1 on early differentiation of hESCs by inducing cells into three different germ layers. For endoderm differentiation, Activin A treatment was used in this study. The cells were cultured in RPMI 1640 basic medium supplemented with B27 (**Figure 6D**). After treating with Activin A for 3 days, cells were collected to detect the expression of endodermal markers FOXA2 and SOX17 by flow cytometry and RT-qPCR. The flow cytometry results showed that $FOXA2^+SOX17^+$double positive cells were significantly increased in the *FUBP3* KO cultures compared with wild-type hESCs after endodermal induction for 3 days (**Figure 6E-F**). However, in FXR2 and L1TD1 KO cultures, the proportion of $FOXA2^+SOX17^+$double positive cells was significantly reduced, indicating that loss of *FUBP3* enhances the ability of hESCs to endodermal differentiation, while loss of *FXR2* and *L1TD1* inhibits the ability to differentiate into endoderm (**Figure 6E-F**). As for hematopoietic mesodermal differentiation, cells were seeded on low attachment plates to form EB spheres, and then cultured in STEMdiff APEL^{TM}2 medium supplemented with factors SCF, BMP4 and VEGF for 6 days (**Figure 6G**). Flow cytometry results showed that *FUBP3*, *FXR2* and *L1TD1* KO hESCs significantly reduced the proportion of mesodermal marker $CD34^+$, indicating that FUBP3, FXR2 and L1TD1 were essential for hematopoietic mesodermal differentiation of hESCs. Deletion of *FUBP3*, *FXR2* and *L1TD1* significantly inhibits the ability to differentiate into mesoderm (**Figure 6H-I**). As for neural ectodermal differentiation, STEMdiff^{TM} neural induction medium with SMADi were used to induce cells to differentiate into neural progenitor cells by monolayer culture protocol (**Figure 6J**). Consistent with the tendency of endoderm differentiation, after neural induction for 3 days, more $SOX1^+$positive cells were present in the *FUBP3* KO cultures compared to wild-type group (**Figure 6K-L**). In *FXR2* and *L1TD1* KO cultures, the proportion of $SOX1^+$positive cells was significantly declined, indicating that loss of *FUBP3* promotes the ability of hESCs to neural ectodermal differentiation, while loss of *FXR2* and *L1TD1* inhibits the ability to ectodermal differentiation (**Figure 6K-L**).

Furthermore, we detected the mRNA expression level of marker genes of three germ layer through RT-qPCR. Consistent with the flow cytometry results, in endoderm differentiation stage, the mRNA expression levels of FOXA2 and SOX17 were significantly increased in *FUBP3* KO cells but decreased in *FXR2* and *L1TD1* KO cells (**Figure 6M**). During the hematopoietic mesoderm differentiation stage, the mRNA expression levels of TBXT (also known as T) and CD34 were all significantly reduced in *FUBP3*, *FXR2* and *L1TD1* KO cells compared to wild-type group (**Figure 6N**). As for neural ectoderm differentiation stage, the mRNA expression levels of neural-ectoderm markers SOX1, PAX6 and NES (also known as NESTIN) were significantly increased in *FUBP3* KO cells but decreased in *FXR2* and *L1TD1* KO cells (**Figure 6O**). These results indicated that FUBP3 may inhibit the endoderm and ectoderm differentiation, but is important for the mesoderm differentiation. FXR2 and L1TD1 genes are crucial for the differentiation of all three germ layers, and absence may significantly affect the differentiation ability of hESCs. In conclusion, the above results revealed that m6A readers play an important role in regulating the early differentiation of hESCs.

Discussion

In recent years, m^6A has emerged as a key RNA modification in various biological processes and diseases [6,7]. Thanks to significant advances in high-throughput sequencing technologies such as MeRIP-seq [1,2] and GLORI [5], systematic mapping of m^6A modification sites and their dynamic changes in different tissues, conditions and cell types has become feasible [3,9-11]. On the other hand, m^6A modification exhibits diverse post-transcriptional functional readouts, including changes in RNA half-life, in translation efficiency, and in alternative splicing [57]. Despite the diverse functional readouts of m^6A, there is a lack of systematic measurement and comparison of m^6A post-transcriptional functional readouts across multiple cell lines. In fact, an extensive search of the public omics database GEO could only yield a very limited number of cell lines where the m^6A methylome could be coupled with its readouts. For example, we obtained the m^6A profiles along with Ribo-seq data for only four cell lines from GEO with acceptable quality (HepG2, HeLa, Huh7, and MOLM13), and these data were introduced as an expanding dataset for translational efficiency readout models.

Even for alternative splicing, which can be measured by RNA-seq, few datasets could meet the required sequencing depth for comprehensive alternative splicing identification. To this end, in this study we first selected five representative cell lines (A549, hESC, HEK293T, JURKAT and HUVEC) and performed temporal transcriptome sequencing, Ribo-seq and ultra-deep RNA sequencing on m^6A-normal (shControl) and m^6A-disrupted (shMETTL3) cells. Our high-throughput data provide a comprehensive resource for further exploration of the regulatory mechanism as well as the key regulatory targets of m^6A methylation. Indeed, machine learning modeling of the profiled m^6A readouts has successfully prioritized novel m^6A readers from the RBP features of the models, demonstrating the utility of m^6A readout profiles.

Noticeable cell type specificity of the m^6A readouts was observed. On the one hand, the m^6A methylation rate alone is not sufficient to explain this diversity. There is at least partial overlap between m^6A target sites and genes between different cell types. However, the m^6A readouts are limited except for some basic pathways. Furthermore, the correlations between GLORI-measured m^6A modification ratios with the post-transcriptional readouts were compromised, and the inclusion of m^6A modification ratio did not result in better prediction of m^6A readouts. Analysis of our machine learning model suggests that the prediction performance was largely contributed by RBP-based features, either the RBP binding site score near the m^6A site or the distance between RBP binding sites and m^6A modification sites. M^6A is characterized by a large number of reader partners compared to other RNA modifications. These readers form a complex regulatory context that controls how the m^6A modification is interpreted in cells. Since the readers themselves have different expression patterns in different cell types, it is intuitively expected that the final readouts of m^6A could differ even at the m^6A site with the different set of available readers. Indeed, we also found that there are few RBPs that contribute to the predictions of all readout types in all cell types. On the other hand, it is likely that cell type specificity is overestimated when compared to the entire repository of human cell types. To be honest, we intentionally selected five cell types from the different cell clades that show distinctive gene expression patterns to ensure representativeness of our data, at an affordable cost to us. In the future, it will be interesting to include similar cell types or cell lines related to the same physiological or disease process for mining the consensus m^6A readout targets and mechanisms.

RBP features contribute significantly to the prediction of m^6A readout in our machine learning models. However, the use of current RBP information should still be done with caution. We observed several RBPs with high importance scores in our models. Although some of these high-scoring RBPs is indeed known m^6A readers or can be validated as new m^6A readers in this study, m^6A RNA pull-down assay of some others returned negative results. This is partly because the current RBP binding site map is far from complete. In order to be comprehensive, we collected and re-analyzed RBP binding site data derived from different techniques, but there is still a significant fraction of RBP binding site maps that have only a few hundred binding sites, which significantly reduces their possible association with m^6A. Even for well-known m^6A reader proteins such as YTHDF1 and YTHDF2, their prominent contribution to m^6A readout prediction can only be achieved when the binding sites from multiple techniques were merged. In particular, we noticed the TRIBE-like techniques (including TRIBE, STAMP, and HyperTRIBE) for RBP binding site mapping in our analysis. Previously, TRIBE and STAMP were successfully applied to the YTHDF target identification [13]. These data were included in our models and contribute significantly to the feature importance scores of YTHDF1 and YTHDF2. We also profiled the binding sites of candidate m^6A readers using HyperTRIBE, which demonstrated the significant overlap between the binding sites of these readers and m^6A methylation target genes in hESC. It is expected that the RBP binding context of m6A will be interpreted in a more comprehensive and less biased manner with the improved methodology and applications of RBP binding site profiling. In addition, for readouts such as exon inclusion ratio changes, we could only observe a compromised fraction of exons that have m^6A sites near their exon boundaries. Analysis of the exon inclusion change prediction model suggests that distance to m^6A site rather than binding score is the best feature set. unlike the prediction models for half-life or translational efficiency changes. These together indicates that an intensive focusing on the local m6A patterns is necessary to explore the m^6A-mediated alternative splicing events.

In this study, we screened DDX6, FUBP3, FXR2 and L1TD1 as the novel m^6A readers, and demonstrated the new regulatory roles of the latter three in hESC early differentiation. DDX6 is an RNA helicase belonging to the Dead Box family. In cancer, DDX6 regulates the expression of oncogenes and tumor suppressor genes by influencing the stability and translation of miRNA [58]. DDX6 plays an important role in maintaining the characteristics of tumor stem cells, enhancing the proliferation and invasion ability of tumor cells, and chemotherapeutic resistance [59-61]. FUBP3 is an

RNA-binding protein that can bind to the far upstream element (FUSE) of specific RNA molecules, thereby regulating gene expression. In cancer, FUBP3 functions as an oncogene or tumor suppressor gene depending on the type and context of the cancer. Studies have shown that FUBP3 may promote tumor growth and metastasis in some cancers [62,63], while in other cases, it may be related to the inhibition of tumor progression [64]. FXR2 is also an RNA-binding protein related to Fragile X syndrome. Studies have shown that in cancer, FXR2 may be related to the inhibition of cancer cell proliferation [65]. The role of L1TD1 in cancer is relatively less studied, but some studies have shown that it may be related to the proliferation and invasion ability of tumor cells, and may serve as a potential prognostic marker in certain cancer types [66].Recent studies have also discovered the regulatory roles of DDX6, FXR2 and L1TD1 on the functions of stem cells. Suppression of RNA helicase DDX6 endows human and mouse primed embryonic stem cells (ESCs) with a differentiation-resistant, "hyper-pluripotent" state, which readily reprograms to a naïve state resembling the preimplantation embryo [56]. FXR2 is regarded as one of the critical regulation proteins of neurogenesis [67]. L1TD1 is confirmed as a part of the pluripotency interactome network of OCT4, SOX2, and NANOG, bridging nuclear and cytoplasmic regulation [68]. Our results uncovered the roles of FUBP3, FXR2 and L1TD1 in hESC differentiation other than self-renewal, underscoring their new roles in stem cell fate control.

Our study also has some limitations. Firstly, the scope of cell types included is not sufficient in comparison with the wide spectrum of human cell atlas. Secondly, recent studies have revealed new layers of m^6A readouts such as regulatory interplay with chromatin, but this aspect was not covered in current study. Thirdly, the molecular mechanism of the identified m^6A readouts have not been in-depth investigated. Nonetheless, our study has provided useful resource to bridge the gap between m^6A methylome landscape and its readouts, and prioritizing interesting novel m^6A readers for stem cell fate control. We expected the future research could expand the range of cell types studied, improve data resources, and delve deeper into the molecular mechanisms underlying m^6A functional readouts.

Data availability

The data can be accessed in Gene Expression Omnibus (https://www.ncbi.nlm.nih.gov/geo) with accessions of GSE179872 (m^6A readout profiling), GSE290408 (GLORI) and GSE287679, GSE288304 (HyperTRIBE).

Funding

This study was supported by the National Natural Science Foundation of China (32222020 and 32070658 to Y.Z., 32371533 to Y.L.), Michigan Medicine-PKUHSC Joint Institute for Translational and Clinical Research (BMU2023JI002 to Y.L.), PKU-Baidu Fund (2019BD014 to Q.C.).

Reference

1. Dominissini, D., Moshitch-Moshkovitz, S., Schwartz, S., Salmon-Divon, M., Ungar, L., Osenberg, S., Cesarkas, K., Jacob-Hirsch, J., Amariglio, N., Kupiec, M., et al. (2012). Topology of the human and mouse m6A RNA methylomes revealed by m6A-seq. Nature *485*, 201-206. 10.1038/nature11112.
2. Meyer, K.D., Saletore, Y., Zumbo, P., Elemento, O., Mason, C.E., and Jaffrey, S.R. (2012). Comprehensive analysis of mRNA methylation reveals enrichment in 3' UTRs and near stop codons. Cell *149*, 1635-1646. 10.1016/j.cell.2012.05.003.
3. Xuan, J., Chen, L., Chen, Z., Pang, J., Huang, J., Lin, J., Zheng, L., Li, B., Qu, L., and Yang, J. (2024). RMBase v3.0: decode the landscape, mechanisms and functions of RNA modifications. Nucleic Acids Res *52*, D273-D284. 10.1093/nar/gkad1070.
4. Ke, S., Alemu, E.A., Mertens, C., Gantman, E.C., Fak, J.J., Mele, A., Haripal, B., Zucker-Scharff, I., Moore, M.J., Park, C.Y., et al. (2015). A majority of m6A residues are in the last exons, allowing the potential for 3' UTR regulation. Genes Dev *29*, 2037-2053. 10.1101/gad.269415.115.
5. Liu, C., Sun, H., Yi, Y., Shen, W., Li, K., Xiao, Y., Li, F., Li, Y., Hou, Y., Lu, B., et al. (2023). Absolute quantification of single-base m(6)A methylation in the mammalian transcriptome using GLORI. Nat Biotechnol *41*, 355-366. 10.1038/s41587-022-01487-9.
6. Deng, X., Qing, Y., Horne, D., Huang, H., and Chen, J. (2023). The roles and implications of RNA m(6)A modification in cancer. Nat Rev Clin Oncol *20*, 507-526. 10.1038/s41571-023-00774-x.
7. Liu, W.W., Zheng, S.Q., Li, T., Fei, Y.F., Wang, C., Zhang, S., Wang, F., Jiang, G.M., and Wang, H. (2024). RNA modifications in cellular metabolism: implications for metabolism-targeted therapy and immunotherapy. Signal Transduct Target Ther *9*, 70. 10.1038/s41392-024-01777-5.

8. Fu, Y., Dominissini, D., Rechavi, G., and He, C. (2014). Gene expression regulation mediated through reversible m6A RNA methylation. Nat Rev Genet *15*, 293-306. 10.1038/nrg3724.

9. Liang, Z., Ye, H., Ma, J., Wei, Z., Wang, Y., Zhang, Y., Huang, D., Song, B., Meng, J., Rigden, D.J., and Chen, K. (2024). m6A-Atlas v2.0: updated resources for unraveling the N6-methyladenosine (m6A) epitranscriptome among multiple species. Nucleic Acids Res *52*, D194-d202. 10.1093/nar/gkad691.

10. Xiao, S., Cao, S., Huang, Q., Xia, L., Deng, M., Yang, M., Jia, G., Liu, X., Shi, J., Wang, W., et al. (2019). The RNA N(6)-methyladenosine modification landscape of human fetal tissues. Nat Cell Biol *21*, 651-661. 10.1038/s41556-019-0315-4.

11. Liu, J., Li, K., Cai, J., Zhang, M., Zhang, X., Xiong, X., Meng, H., Xu, X., Huang, Z., Peng, J., et al. (2020). Landscape and Regulation of m(6)A and m(6)Am Methylome across Human and Mouse Tissues. Mol Cell *77*, 426-440 e426. 10.1016/j.molcel.2019.09.032.

12. Shi, H., Wei, J., and He, C. (2019). Where, When, and How: Context-Dependent Functions of RNA Methylation Writers, Readers, and Erasers. Mol Cell *74*, 640-650. 10.1016/j.molcel.2019.04.025.

13. Flamand, M.N., Ke, K., Tamming, R., and Meyer, K.D. (2022). Single-molecule identification of the target RNAs of different RNA binding proteins simultaneously in cells. Genes Dev *36*, 1002-1015. 10.1101/gad.349983.122.

14. Zaccara, S., and Jaffrey, S.R. (2020). A Unified Model for the Function of YTHDF Proteins in Regulating m(6)A-Modified mRNA. Cell *181*, 1582-1595.e1518. 10.1016/j.cell.2020.05.012.

15. Wang, X., Lu, Z., Gomez, A., Hon, G.C., Yue, Y., Han, D., Fu, Y., Parisien, M., Dai, Q., Jia, G., et al. (2014). N6-methyladenosine-dependent regulation of messenger RNA stability. Nature *505*, 117-120. 10.1038/nature12730.

16. Wang, X., Zhao, B.S., Roundtree, I.A., Lu, Z., Han, D., Ma, H., Weng, X., Chen, K., Shi, H., and He, C. (2015). N(6)-methyladenosine Modulates Messenger RNA Translation Efficiency. Cell *161*, 1388-1399. 10.1016/j.cell.2015.05.014.

17. Xiao, W., Adhikari, S., Dahal, U., Chen, Y.S., Hao, Y.J., Sun, B.F., Sun, H.Y., Li, A., Ping, X.L., Lai, W.Y., et al. (2016). Nuclear m(6)A Reader YTHDC1 Regulates mRNA Splicing. Mol Cell *61*, 507-519. 10.1016/j.molcel.2016.01.012.

18. Huang, H., Weng, H., Sun, W., Qin, X., Shi, H., Wu, H., Zhao, B.S., Mesquita, A., Liu, C., Yuan, C.L., et al. (2018). Recognition of RNA N(6)-methyladenosine by IGF2BP proteins enhances mRNA stability and translation. Nat Cell Biol *20*, 285-295. 10.1038/s41556-018-0045-z.

19. Li, M., Zhao, X., Wang, W., Shi, H., Pan, Q., Lu, Z., Perez, S.P., Suganthan, R., He, C., Bjoras, M., and Klungland, A. (2018). Ythdf2-mediated m(6)A mRNA clearance modulates neural development in mice. Genome Biol *19*, 69. 10.1186/s13059-018-1436-y.

20. Bai, Y., Yang, C., Wu, R., Huang, L., Song, S., Li, W., Yan, P., Lin, C., Li, D., and Zhang, Y. (2019). YTHDF1 Regulates Tumorigenicity and Cancer Stem Cell-Like Activity in Human Colorectal Carcinoma. Front Oncol *9*, 332. 10.3389/fonc.2019.00332.

21. Kasowitz, S.D., Ma, J., Anderson, S.J., Leu, N.A., Xu, Y., Gregory, B.D., Schultz, R.M., and Wang, P.J. (2018). Nuclear m6A reader YTHDC1 regulates alternative polyadenylation and splicing during mouse oocyte development. PLoS Genet *14*, e1007412. 10.1371/journal.pgen.1007412.

22. Edupuganti, R.R., Geiger, S., Lindeboom, R.G.H., Shi, H., Hsu, P.J., Lu, Z., Wang, S.Y., Baltissen, M.P.A., Jansen, P., Rossa, M., et al. (2017). N(6)-methyladenosine (m(6)A) recruits and repels proteins to regulate mRNA homeostasis. Nat Struct Mol Biol *24*, 870-878. 10.1038/nsmb.3462.

23. Visvanathan, A., Patil, V., Arora, A., Hegde, A.S., Arivazhagan, A., Santosh, V., and Somasundaram, K. (2018). Essential role of METTL3-mediated m(6)A modification in glioma stem-like cells maintenance and radioresistance. Oncogene *37*, 522-533. 10.1038/onc.2017.351.

24. McMillan, M., Gomez, N., Hsieh, C., Bekier, M., Li, X., Miguez, R., Tank, E.M.H., and Barmada, S.J. (2023). RNA methylation influences TDP43 binding and disease pathogenesis in models of amyotrophic lateral sclerosis and frontotemporal dementia. Mol Cell *83*, 219-236.e217. 10.1016/j.molcel.2022.12.019.

25. Batista, P.J., Molinie, B., Wang, J., Qu, K., Zhang, J., Li, L., Bouley, D.M., Lujan, E., Haddad, B., Daneshvar, K., et al. (2014). m(6)A RNA modification controls cell fate transition in mammalian embryonic stem cells. Cell Stem Cell *15*, 707-719. 10.1016/j.stem.2014.09.019.

26. Geula, S., Moshitch-Moshkovitz, S., Dominissini, D., Mansour, A.A., Kol, N., Salmon-Divon, M., Hershkovitz, V., Peer, E., Mor, N., Manor, Y.S., et al. (2015). Stem cells. m6A mRNA methylation facilitates resolution of naïve pluripotency toward differentiation. Science *347*, 1002-1006. 10.1126/science.1261417.

27. Zhang, M., Zhai, Y., Zhang, S., Dai, X., and Li, Z. (2020). Roles of N6-Methyladenosine (m(6)A) in Stem Cell Fate Decisions and Early Embryonic Development in Mammals. Front Cell Dev Biol *8*, 782. 10.3389/fcell.2020.00782.

28. Chen, T., Hao, Y.J., Zhang, Y., Li, M.M., Wang, M., Han, W., Wu, Y., Lv, Y., Hao, J., Wang, L., et al. (2015). m(6)A RNA methylation is regulated by microRNAs and promotes reprogramming to pluripotency. Cell Stem Cell *16*, 289-301. 10.1016/j.stem.2015.01.016.

29. Wang, Y., Li, Y., Toth, J.I., Petroski, M.D., Zhang, Z., and Zhao, J.C. (2014). N6-methyladenosine modification destabilizes developmental regulators in embryonic stem cells. Nat Cell Biol *16*, 191-198. 10.1038/ncb2902.

30. Wen, J., Lv, R., Ma, H., Shen, H., He, C., Wang, J., Jiao, F., Liu, H., Yang, P., Tan, L., et al. (2018). Zc3h13 Regulates Nuclear RNA m(6)A Methylation and Mouse Embryonic Stem Cell Self-Renewal. Mol Cell *69*, 1028-1038.e1026. 10.1016/j.molcel.2018.02.015.

31. Lasman, L., Krupalnik, V., Viukov, S., Mor, N., Aguilera-Castrejon, A., Schneir, D., Bayerl, J., Mizrahi, O., Peles, S., Tawil, S., et al. (2020). Context-dependent functional compensation between Ythdf m(6)A reader proteins. Genes Dev *34*, 1373-1391. 10.1101/gad.340695.120.

32. Liu, J., Gao, M., He, J., Wu, K., Lin, S., Jin, L., Chen, Y., Liu, H., Shi, J., Wang, X., et al. (2021). The RNA m(6)A reader YTHDC1 silences retrotransposons and guards ES cell identity. Nature *591*, 322-326. 10.1038/s41586-021-03313-9.

33. Bertero, A., Brown, S., Madrigal, P., Osnato, A., Ortmann, D., Yiangou, L., Kadiwala, J., Hubner, N.C., de Los Mozos, I.R., Sadée, C., et al. (2018). The SMAD2/3 interactome reveals that TGFβ controls m(6)A mRNA methylation in pluripotency. Nature *555*, 256-259. 10.1038/nature25784.

34. Han, Z., Xu, Z., Yu, Y., Cao, Y., Bao, Z., Gao, X., Ye, D., Yan, G., Gong, R., Xu, J., et al. (2021). ALKBH5-mediated m(6)A mRNA methylation governs human embryonic stem cell cardiac commitment. Mol Ther Nucleic Acids *26*, 22-33. 10.1016/j.omtn.2021.05.019.

35. Baudin, B., Bruneel, A., Bosselut, N., and Vaubourdolle, M. (2007). A protocol for isolation and culture of human umbilical vein endothelial cells. Nat Protoc *2*, 481-485. 10.1038/nprot.2007.54.

36. Ingolia, N.T., Brar, G.A., Rouskin, S., McGeachy, A.M., and Weissman, J.S. (2012). The ribosome profiling strategy for monitoring translation in vivo by deep sequencing of ribosome-protected mRNA fragments. Nat Protoc *7*, 1534-1550. 10.1038/nprot.2012.086.

37. Xiao, Z., Zou, Q., Liu, Y., and Yang, X. (2016). Genome-wide assessment of differential translations with ribosome profiling data. Nat Commun *7*, 11194. 10.1038/ncomms11194.

38. Wang, Y., Xie, Z., Kutschera, E., Adams, J.I., Kadash-Edmondson, K.E., and Xing, Y. (2024). rMATS-turbo: an efficient and flexible computational tool for alternative splicing analysis of large-scale RNA-seq data. Nat Protoc *19*, 1083-1104. 10.1038/s41596-023-00944-2.

39. Wu, T., Hu, E., Xu, S., Chen, M., Guo, P., Dai, Z., Feng, T., Zhou, L., Tang, W., Zhan, L., et al. (2021). clusterProfiler 4.0: A universal enrichment tool for interpreting omics data. Innovation (Camb) *2*, 100141. 10.1016/j.xinn.2021.100141.

40. Tsherniak, A., Vazquez, F., Montgomery, P.G., Weir, B.A., Kryukov, G., Cowley, G.S., Gill, S., Harrington, W.F., Pantel, S., Krill-Burger, J.M., et al. (2017). Defining a Cancer Dependency Map. Cell *170*, 564-576.e516. 10.1016/j.cell.2017.06.010.

41. Meng, J., Lu, Z., Liu, H., Zhang, L., Zhang, S., Chen, Y., Rao, M.K., and Huang, Y. (2014). A protocol for RNA methylation differential analysis with MeRIP-Seq data and exomePeak R/Bioconductor package. Methods *69*, 274-281. 10.1016/j.ymeth.2014.06.008.

42. Zhu, Y., Xu, G., Yang, Y.T., Xu, Z., Chen, X., Shi, B., Xie, D., Lu, Z.J., and Wang, P. (2019). POSTAR2: deciphering the post-transcriptional regulatory logics. Nucleic Acids Res *47*, D203-d211. 10.1093/nar/gky830.

43. Uren, P.J., Bahrami-Samani, E., Burns, S.C., Qiao, M., Karginov, F.V., Hodges, E., Hannon, G.J., Sanford, J.R., Penalva, L.O., and Smith, A.D. (2012). Site identification in high-throughput RNA-protein interaction data. Bioinformatics *28*, 3013-3020. 10.1093/bioinformatics/bts569.

44. Van Nostrand, E.L., Freese, P., Pratt, G.A., Wang, X., Wei, X., Xiao, R., Blue, S.M., Chen, J.Y., Cody, N.A.L., Dominguez, D., et al. (2020). A large-scale binding and functional map of human RNA-binding proteins. Nature *583*, 711-719. 10.1038/s41586-020-2077-3.

45. GTEx Consortium (2020). The GTEx Consortium atlas of genetic regulatory effects across human tissues. Science *369*, 1318-1330. 10.1126/science.aaz1776.

46. Chen, T., and Guestrin, C. (2016). XGBoost: A Scalable Tree Boosting System. Proceedings of the 22nd ACM SIGKDD International Conference on Knowledge Discovery and Data Mining. Association for Computing Machinery.

47. Li, J., He, S., Guo, F., and Zou, Q. (2021). HSM6AP: a high-precision predictor for the Homo sapiens N6-methyladenosine (m^6 A) based on multiple weights and feature stitching. RNA Biol *18*, 1882-1892. 10.1080/15476286.2021.1875180.

48. Zhou, J., You, D., Bai, J., Chen, X., Wu, Y., Wang, Z., Tang, Y., Zhao, Y., and Feng, G. (2023). Machine Learning Methods in Real-World Studies of Cardiovascular Disease. Cardiovasc Innov Appl *7*, CVIA.2023.0011.

49. Rahman, R., Xu, W., Jin, H., and Rosbash, M. (2018). Identification of RNA-binding protein targets with HyperTRIBE. Nat Protoc *13*, 1829-1849. 10.1038/s41596-018-0020-y.

50. Biswas, J., Rosbash, M., Singer, R.H., and Rahman, R. (2021). Protocol for using TRIBE to study RNA-protein interactions and nuclear organization in mammalian cells. STAR Protoc *2*, 100634. 10.1016/j.xpro.2021.100634.

51. Heinz, S., Benner, C., Spann, N., Bertolino, E., Lin, Y.C., Laslo, P., Cheng, J.X., Murre, C., Singh, H., and Glass, C.K. (2010). Simple combinations of lineage-determining transcription factors prime cis-regulatory elements required for macrophage and B cell identities. Mol Cell *38*, 576-589. 10.1016/j.molcel.2010.05.004.

52. Ramírez, F., Dündar, F., Diehl, S., Grüning, B.A., and Manke, T. (2014). deepTools: a flexible platform for exploring deep-sequencing data. Nucleic Acids Res *42*, W187-191. 10.1093/nar/gku365.

53. Zhu, H., and Kaufman, D.S. (2019). An Improved Method to Produce Clinical-Scale Natural Killer Cells from Human Pluripotent Stem Cells. Methods Mol Biol *2048*, 107-119. 10.1007/978-1-4939-9728-2_12.

54. McMahon, A.C., Rahman, R., Jin, H., Shen, J.L., Fieldsend, A., Luo, W., and Rosbash, M. (2016). TRIBE: Hijacking an RNA-Editing Enzyme to Identify Cell-Specific Targets of RNA-Binding Proteins. Cell *165*, 742-753. 10.1016/j.cell.2016.03.007.

55. Xu, W., Rahman, R., and Rosbash, M. (2018). Mechanistic implications of enhanced editing by a HyperTRIBE RNA-binding protein. RNA *24*, 173-182. 10.1261/rna.064691.117.

56. Di Stefano, B., Luo, E.C., Haggerty, C., Aigner, S., Charlton, J., Brumbaugh, J., Ji, F., Rabano Jiménez, I., Clowers, K.J., Huebner, A.J., et al. (2019). The RNA Helicase DDX6 Controls Cellular Plasticity by Modulating P-Body Homeostasis. Cell Stem Cell *25*, 622-638.e613. 10.1016/j.stem.2019.08.018.

57. Yang, Y., Hsu, P.J., Chen, Y.S., and Yang, Y.G. (2018). Dynamic transcriptomic m(6)A decoration: writers, erasers, readers and functions in RNA metabolism. Cell Res *28*, 616-624. 10.1038/s41422-018-0040-8.

58. Iio, A., Takagi, T., Miki, K., Naoe, T., Nakayama, A., and Akao, Y. (2013). DDX6 post-transcriptionally down-regulates miR-143/145 expression through host gene NCR143/145 in cancer cells. Biochim Biophys Acta *1829*, 1102-1110. 10.1016/j.bbagrm.2013.07.010.

59. Cho, Y.J., Kang, W., Kim, S.H., Sa, J.K., Kim, N., Paddison, P.J., Kim, M., Joo, K.M., Hwang, Y.I., and Nam, D.H. (2016). Involvement of DDX6 gene in radio- and chemoresistance in glioblastoma. Int J Oncol *48*, 1053-1062. 10.3892/ijo.2016.3328.

60. Taniguchi, K., Iwatsuki, A., Sugito, N., Shinohara, H., Kuranaga, Y., Oshikawa, Y., Tajirika, T., Futamura, M., Yoshida, K., Uchiyama, K., and Akao, Y. (2018). Oncogene RNA helicase DDX6 promotes the process of c-Myc expression in gastric cancer cells. Mol Carcinog *57*, 579-589. 10.1002/mc.22781.

61. Yao, G., Yu, S., Hou, F., Xiao, Z., Li, G., Ji, X., and Wang, J. (2024). Rab3B enhances the stabilization of DDX6 to promote lung adenocarcinoma aggressiveness. Mol Med *30*, 75. 10.1186/s10020-024-00848-1.

62. Gao, Q., Zhou, R., Meng, Y., Duan, R., Wu, L., Li, R., Deng, F., Lin, C., and Zhao, L. (2020). Long noncoding RNA CMPK2 promotes colorectal cancer progression by activating the FUBP3-c-Myc axis. Oncogene *39*, 3926-3938. 10.1038/s41388-020-1266-8.

63. Sharma, M., Anandram, S., Ross, C., and Srivastava, S. (2023). FUBP3 regulates chronic myeloid leukaemia progression through PRC2 complex regulated PAK1-ERK signalling. J Cell Mol Med *27*, 15-29. 10.1111/jcmm.17584.

64. Yao, Q., Xie, Y., Xu, D., Qu, Z., Wu, J., Zhou, Y., Wei, Y., Xiong, H., and Zhang, X.L. (2022). Lnc-EST12, which is negatively regulated by mycobacterial EST12, suppresses antimycobacterial innate immunity through its interaction with FUBP3. Cell Mol Immunol *19*, 883-897. 10.1038/s41423-022-00878-x.

65. Zeng, W., Zhu, J.F., Guo, J., Huang, G.J., Ai, L.S., Zeng, Y., and Liao, W.J. (2022). m(6)A-modified circFNDC3B inhibits colorectal cancer stemness and metastasis via RNF41-dependent ASB6 degradation. Cell Death Dis *13*, 1008. 10.1038/s41419-022-05451-y.

66. Chakroborty, D., Emani, M.R., Klén, R., Böckelman, C., Hagström, J., Haglund, C., Ristimäki, A., Lahesmaa, R., and Elo, L.L. (2019). L1TD1 - a prognostic marker for colon cancer. BMC Cancer *19*, 727. 10.1186/s12885-019-5952-2.

67. Guo, W., Zhang, L., Christopher, D.M., Teng, Z.Q., Fausett, S.R., Liu, C., George, O.L., Klingensmith, J., Jin, P., and Zhao, X. (2011). RNA-binding protein FXR2 regulates adult hippocampal neurogenesis by reducing Noggin expression. Neuron *70*, 924-938. 10.1016/j.neuron.2011.03.027.

68. Emani, M.R., Närvä, E., Stubb, A., Chakroborty, D., Viitala, M., Rokka, A., Rahkonen, N., Moulder, R., Denessiouk, K., Trokovic, R., et al. (2015). The L1TD1 protein interactome reveals the importance of post-transcriptional regulation in human pluripotency. Stem Cell Reports *4*, 519-528. 10.1016/j.stemcr.2015.01.014.

Figures

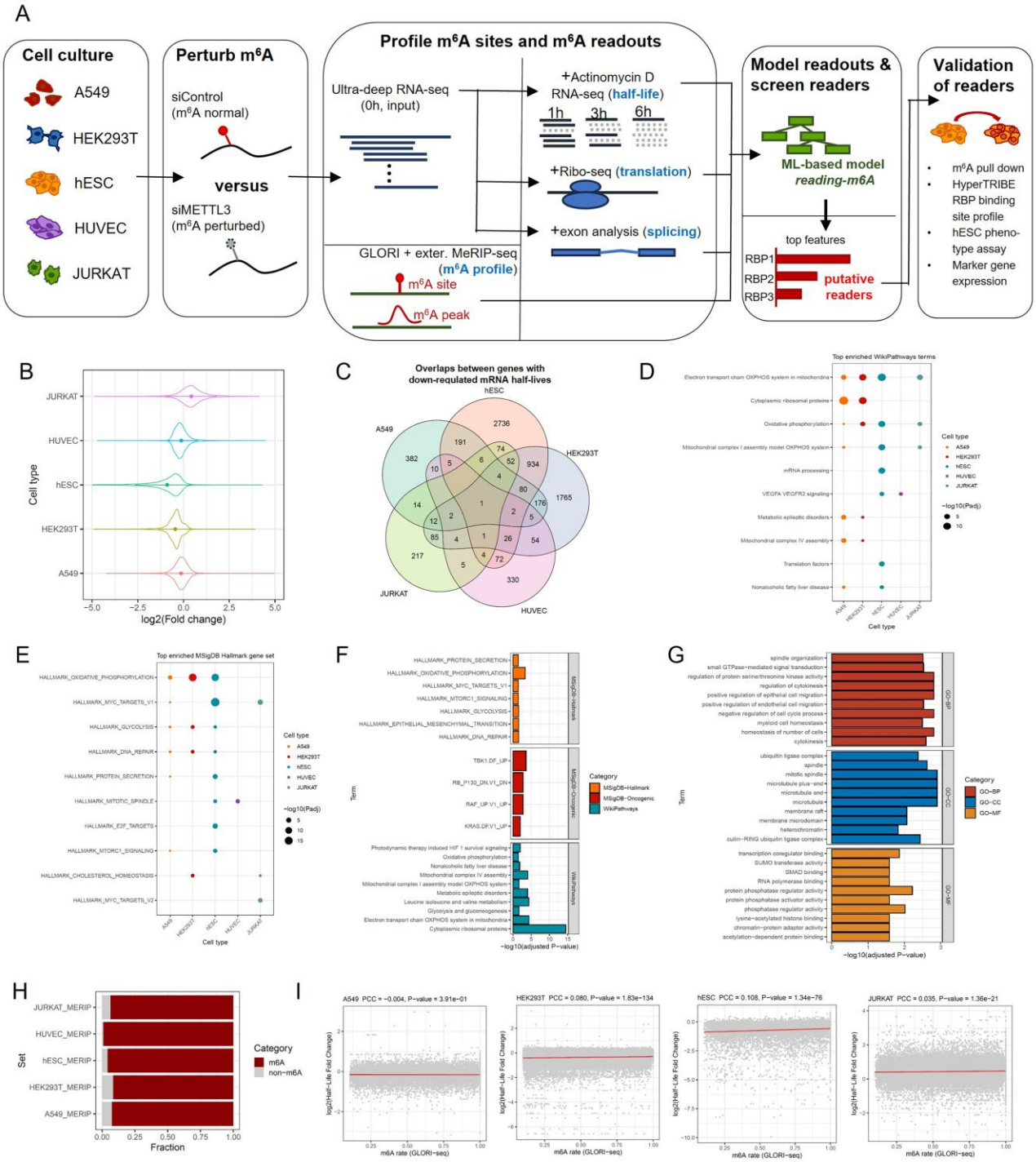

Figure 1. Overview of the experimental design for m^{6}A readout profiling and the half-life readout profiling results.

(A) Overview of the experimental design for m^6A readout profiling. (B) Overview of m^6A-mediated half-life changes. The comparison was performed between m^6A-normal cells (shControl) versus m^6A-disrupted cells (shMETTL3) as the background. (C) Venn diagram of half-life down-regulated genes in different cell types. (D) Top 10 enriched pathways of half-life down-regulated genes among different cell types sorted by total -log10(FDR). The pathway annotation was retrieved from Wikipathways. (E) Top 10 enriched MSigDB Hallmark gene sets of half-life down-regulated genes among different cell types. (F) Top enriched pathways and gene sets for half-life down-regulated genes in A549 cells. (G) Top enriched GO functional terms for half-life down-regulated genes in HUVEC cells. (H) Percentage of half-life down-regulated genes with m^6A methylation peaks identified by MeRIP-seq assay on the corresponding cell types. (I) Correlation between fold change in half-life and m^6A methylation levels assessed by GLORI.

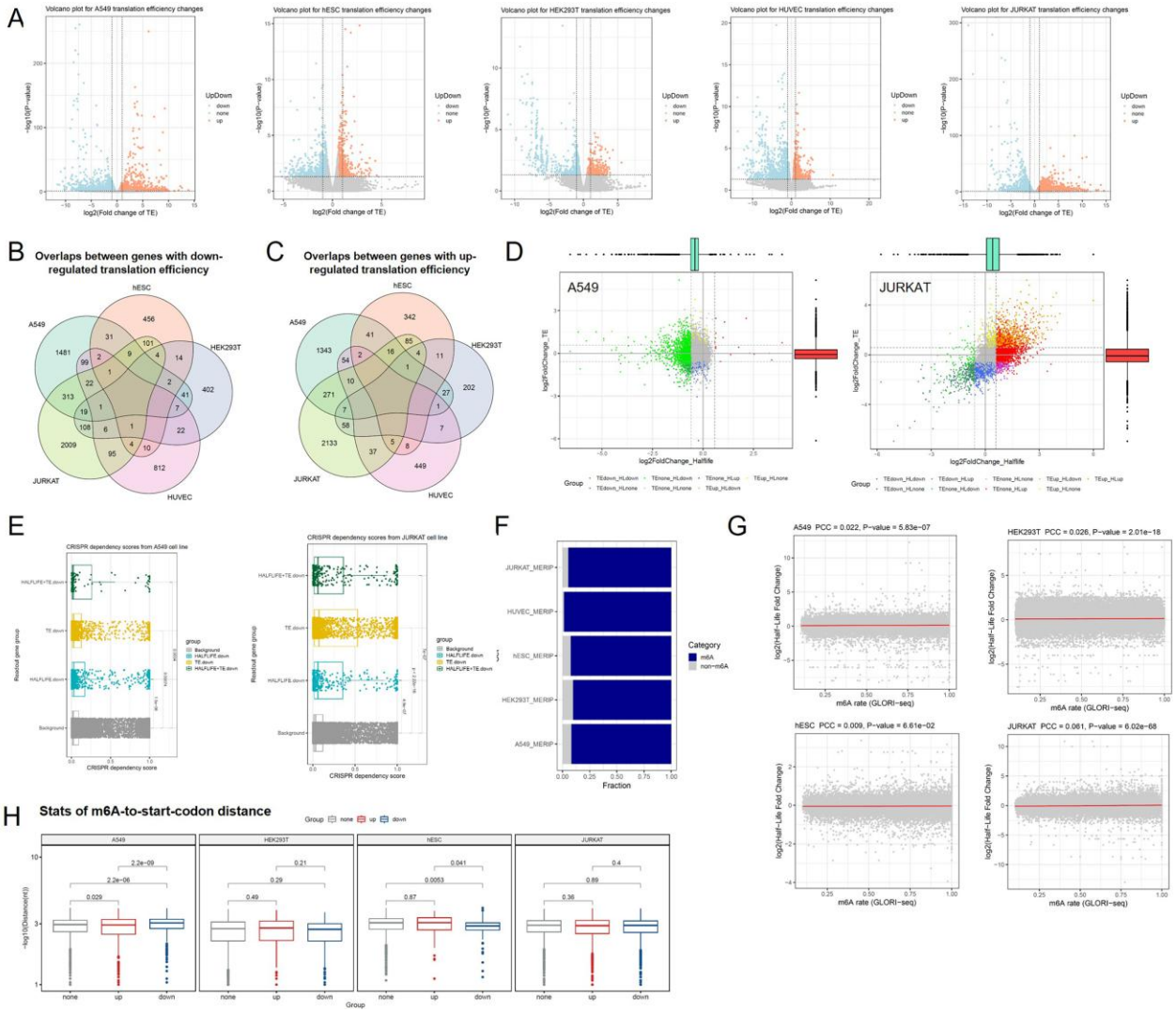

Figure 2. m^{6}A methylation regulates translational efficiency in different cell types.

(A) Volcano plot of m^{6}A-mediated changes in translational efficiency. The comparison was performed between m^{6}A-normal cells (shControl) versus m^{6}A-disrupted cells (shMETTL3) as the background. (B-C) Venn diagram of translational efficiency down-regulated (B) and up-regulated (C) genes in different cell types. (D) Scatter plot showing translational efficiency versus half-life changes in A549 and JURKAT cells. (E) CRISPR-based gene importance scores of genes with half-life and/or translation efficiency changes in cancer cell lines A549 and JURKAT compared to genome background. (F) Percentage of translation efficiency change genes with m^{6}A methylation peaks identified by MeRIP-seq assay on the corresponding cell types. (G) Correlation between fold change in translation efficiency (in absolute values) and m^{6}A methylation levels assessed by GLORI. (H) Box plots comparing the minimum m6A-site-to-strart-codon distance between genes showing different translational efficiency changes.

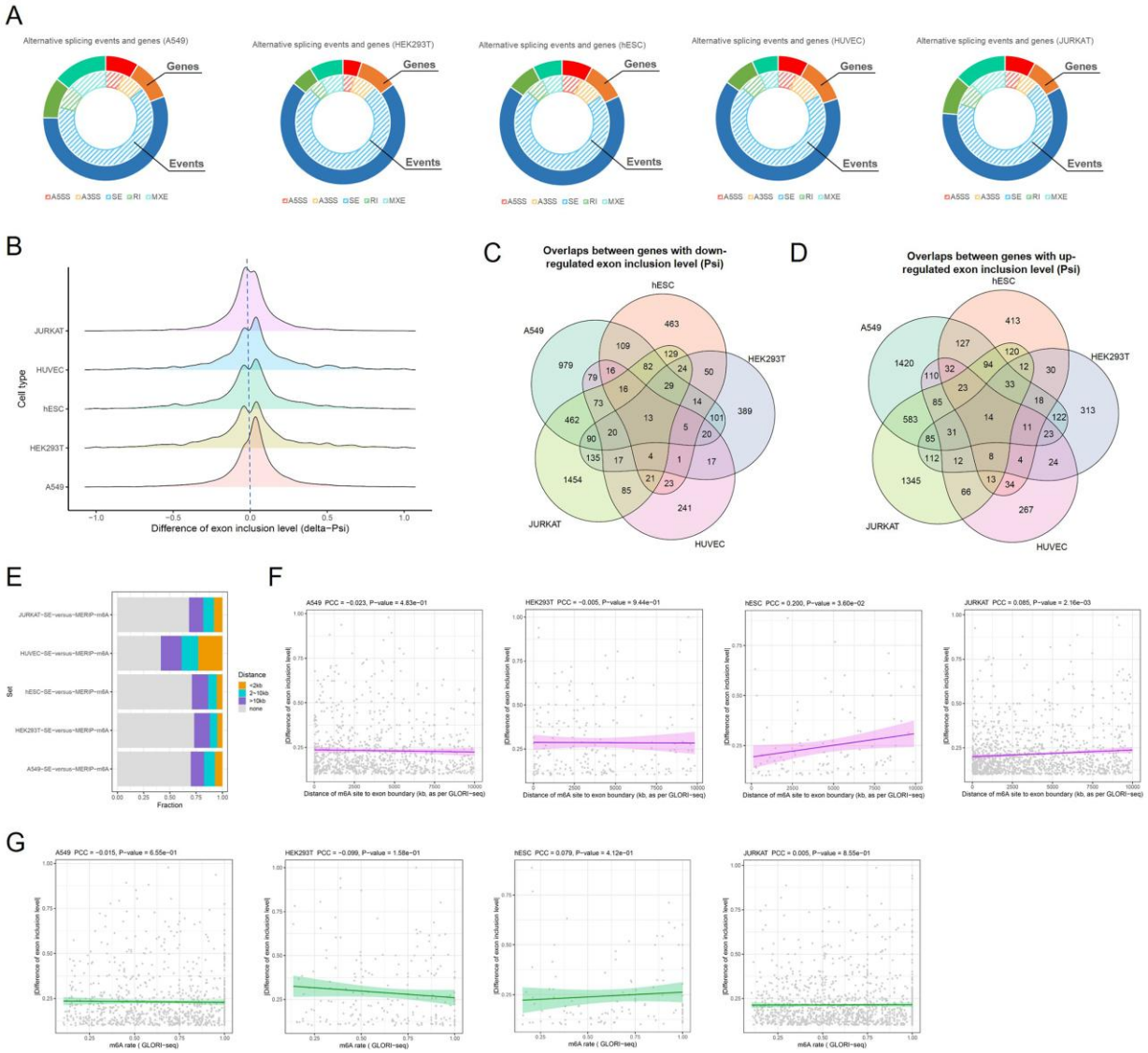

Figure 3. m^{6}A methylation regulates alternative splicing in different cell types.

(A) Circular plot summarizing different types of alternative splicing changes mediated by m^{6}A. The inner and outer loops representing the statistics of the percentage of alternative splicing events and genes, respectively. (B) Ridge plot summarizing the m^{6}A-mediated exon inclusion ratio (Psi) changes. The comparison was performed between m^{6}A-normal cells (shControl) versus m^{6}A-disrupted cells (shMETTL3) as the background. (C-D) Venn diagram of exon inclusion ratio down-regulated (C) and up-regulated (D) genes in different cell types. (E) Percentage of exons showing exon inclusion ratio changes with m^{6}A methylation peaks (identified by MeRIP-seq assay on the corresponding cell types) near their exon boundaries. (F) Correlation between changes in exon inclusion ratio (in absolute values) and m^{6}A (within 10 kb exon boundary) methylation levels assessed by GLORI. (G) Correlation between changes in exon inclusion ratio (in absolute values) and the nearest distances from m^{6}A (within 10 kb exon boundary) methylation sites to exon boundaries.

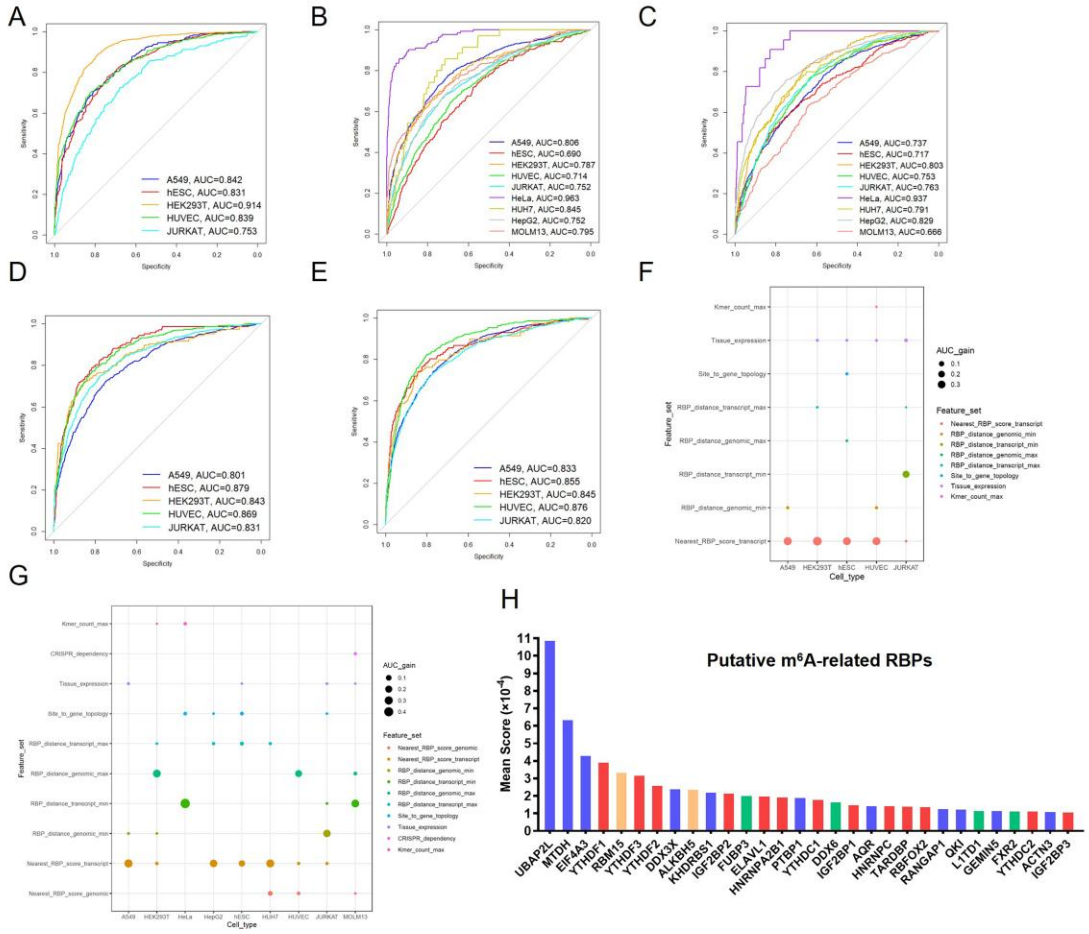

Figure 4. Machine learning models of m^{6}A readouts and their top predictive features.

(A-E) ROC curve assessing the performances of machine learning models (termed as Reading-m^{6}A) for predicting the m^{6}A readout effects in terms of half-life down-regulated genes (A), translational efficiency down-regulated genes (B), translational efficiency up-regulated genes (C), exon inclusion ratio down-regulated exons (D), and exon inclusion ratio up-regulated exons (E) in different cell types. (F) Bubble plot summarizing the performance contributions (as evaluated by the gain of area under ROC curve, AUC) of different feature sets for predicting half-life down-regulated genes. (G) Bubble plot summarizing the performance contributions of different feature sets for predicting translational efficiency down-regulated genes. (H) Bar plot summarizing the RNA binding proteins (RBPs) with high feature importance score in the machine learning models, where red color indicates known m^{6}A readers, orange color indicates known m^{6}A writers/erasers, green color indicates the newly identified m^{6}A reader in this study (FUBP3, DDX6, L1TD1 and FXR2), and blue color indicates the RBPs showing no significant m^{6}A binding ability in our RNA pull-down assay.

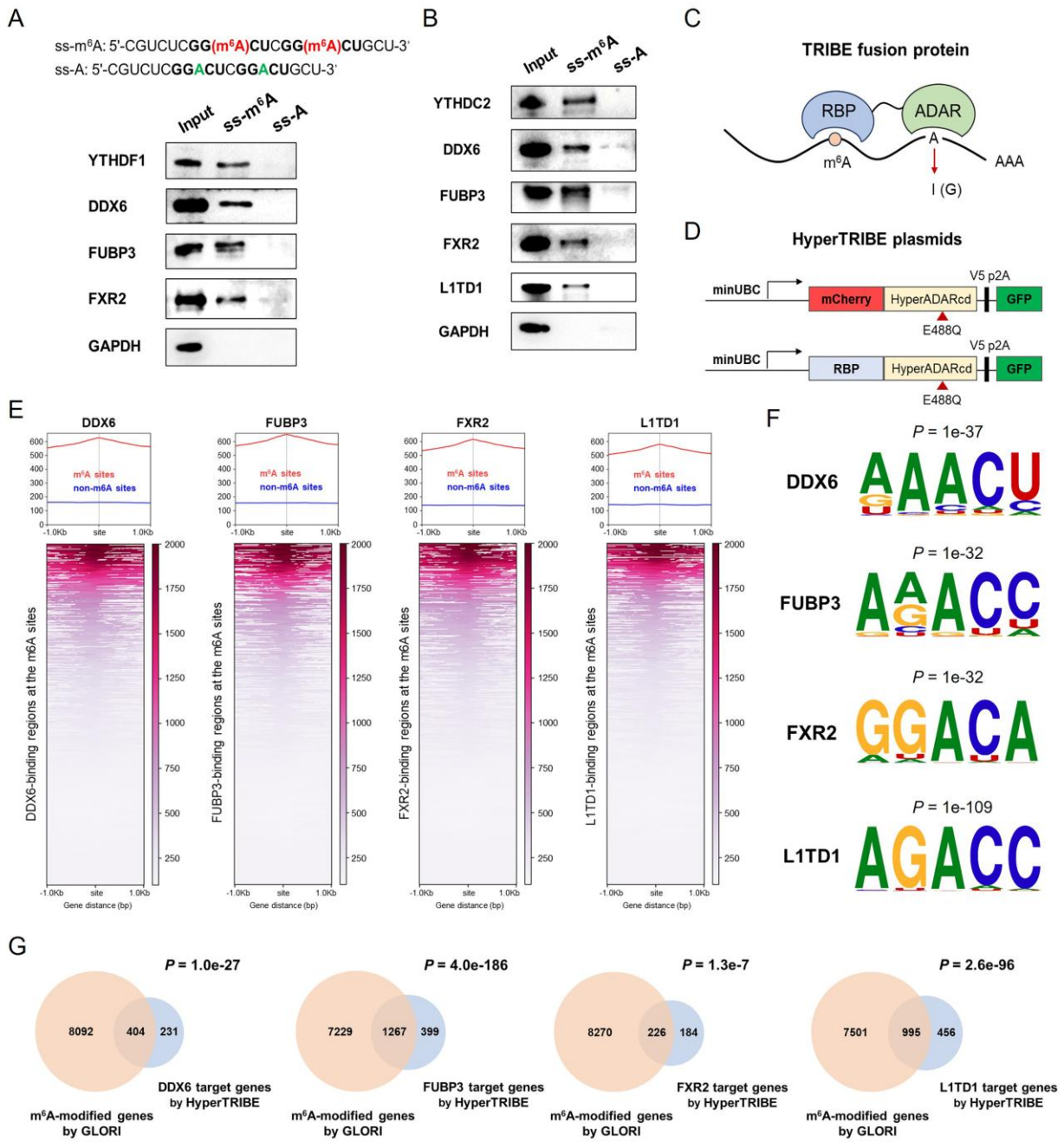

Figure 5. Identification of m^{6}A readers in hESCs.

(A) RNA pull-down assays that verify the binding of RBPs to m^{6}A in A549 cells. (B) RNA pull-down assays that verify the binding of RBPs to m^{6}A in hESCs. (C) Overview of principle of the TRIBE/HyperTRIBE for transcriptome-wide identification of RBP binding sites. (D) Diagram of plasmid constructs for HyperTRIBE. (E) Heatmap showing the distribution of HyperTRIBE-identified RBP binding sites near the m^{6}A methylation sites determined by GLORI in hESCs. (F) DRACH-like motifs in the proximal sequences of RBP binding sites in hESCs.

(G) Venn diagram showing the intersection between RBP target genes identified by HyperTRIBE and m^6A target genes identified by GLORI in hESCs.

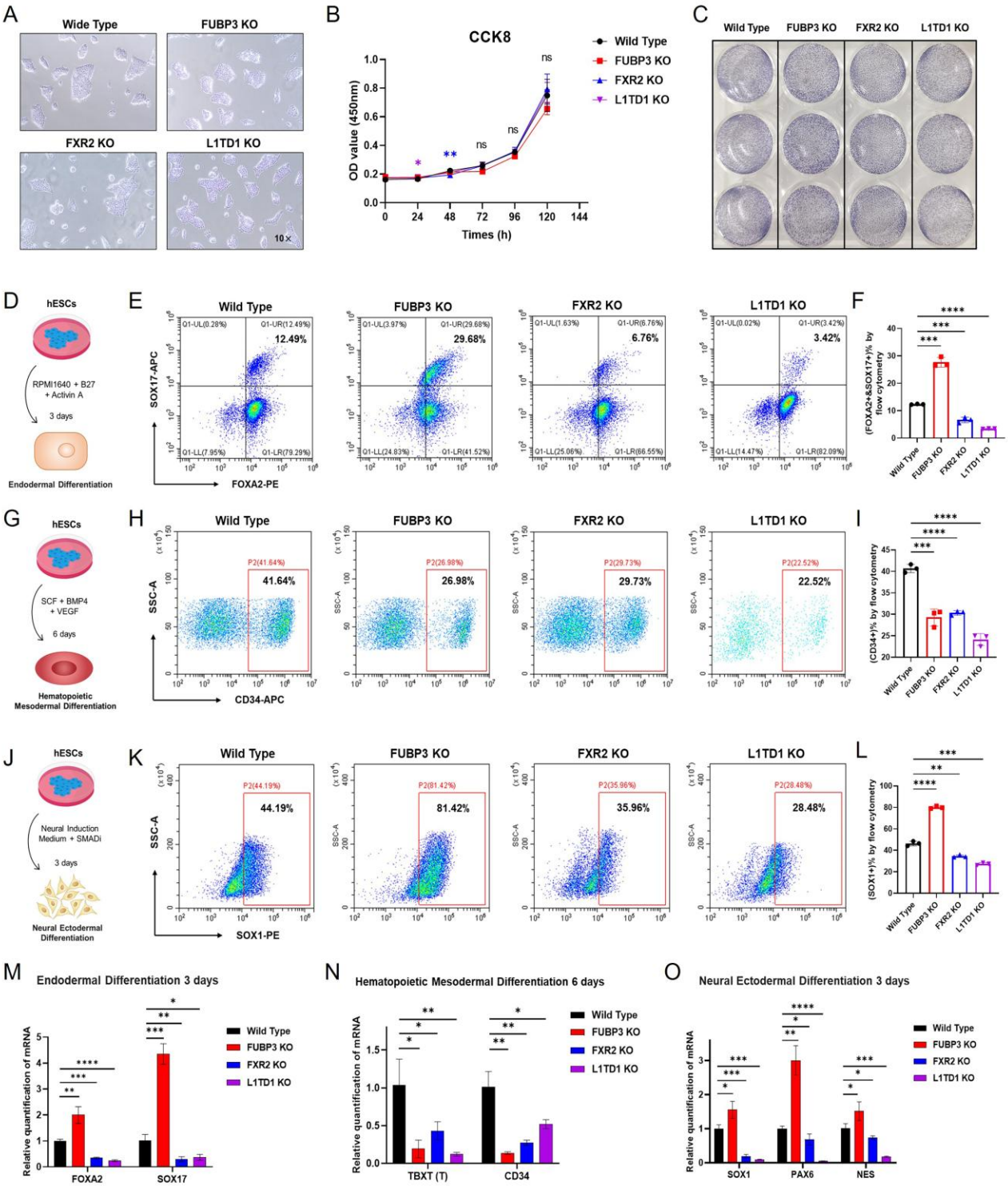

Figure 6. Assessment of m^{6}A readers' regulatory effects on hESC proliferation and differentiation.

(A) Representative images of morphology of WT versus *FUBP3*, *FXR2* and *L1TD1* KO hESCs under bright field. (B) Growth curve assessing cell proliferation kinetics of *FUBP3*, *FXR2* and *L1TD1* KO versus WT hESCs. * means $P < 0.05$, ** means $P < 0.01$, ns means not significant. (C) Alkaline phosphatase (ALP) staining assay of WT versus *FUBP3*, *FXR2* and *L1TD1* KO hESCs. (D) Schematic representation of the induction endodermal differentiation experiment of hESCs. (E-F) Flow cytometry and statistical histogram analysis of endodermal differentiation of WT versus *FUBP3*, *FXR2* and *L1TD1* KO hESCs. *** means $P < 0.001$, **** means $P < 0.0001$. (G) Schematic representation of the induction hematopoietic mesodermal differentiation experiment of hESCs. (H-I) Flow cytometry and statistical histogram analysis of hematopoietic mesodermal differentiation of WT versus *FUBP3*, *FXR2* and *L1TD1* KO hESCs. *** means $P < 0.001$, **** means $P < 0.0001$. (J) Schematic representation of the induction neural ectodermal differentiation experiment of hESCs. (K-L) Flow cytometry and statistical histogram analysis of neural ectodermal differentiation of WT versus *FUBP3*, *FXR2* and *L1TD1* KO hESCs. ** means $P < 0.01$, *** means $P < 0.001$, **** means $P < 0.0001$. (M-O) RT-qPCR analysis of definitive endoderm markers SOX17, FOXA2 (M); mesoderm marker TBXT (also known as T) and CD34 (N); and neural-ectoderm markers SOX1, PAX6, NES in WT versus *FUBP3*, *FXR2* and *L1TD1* KO hESCs. * means $P < 0.05$, ** means $P < 0.01$, *** means $P < 0.001$, **** means $P < 0.0001$ (O). Figures in (D), (G) and (J) were drawn by using pictures from Biovisart (https://biovisart.com.cn) and Bioicons (https://bioicons.com/) with permission.

Supplementary Figures

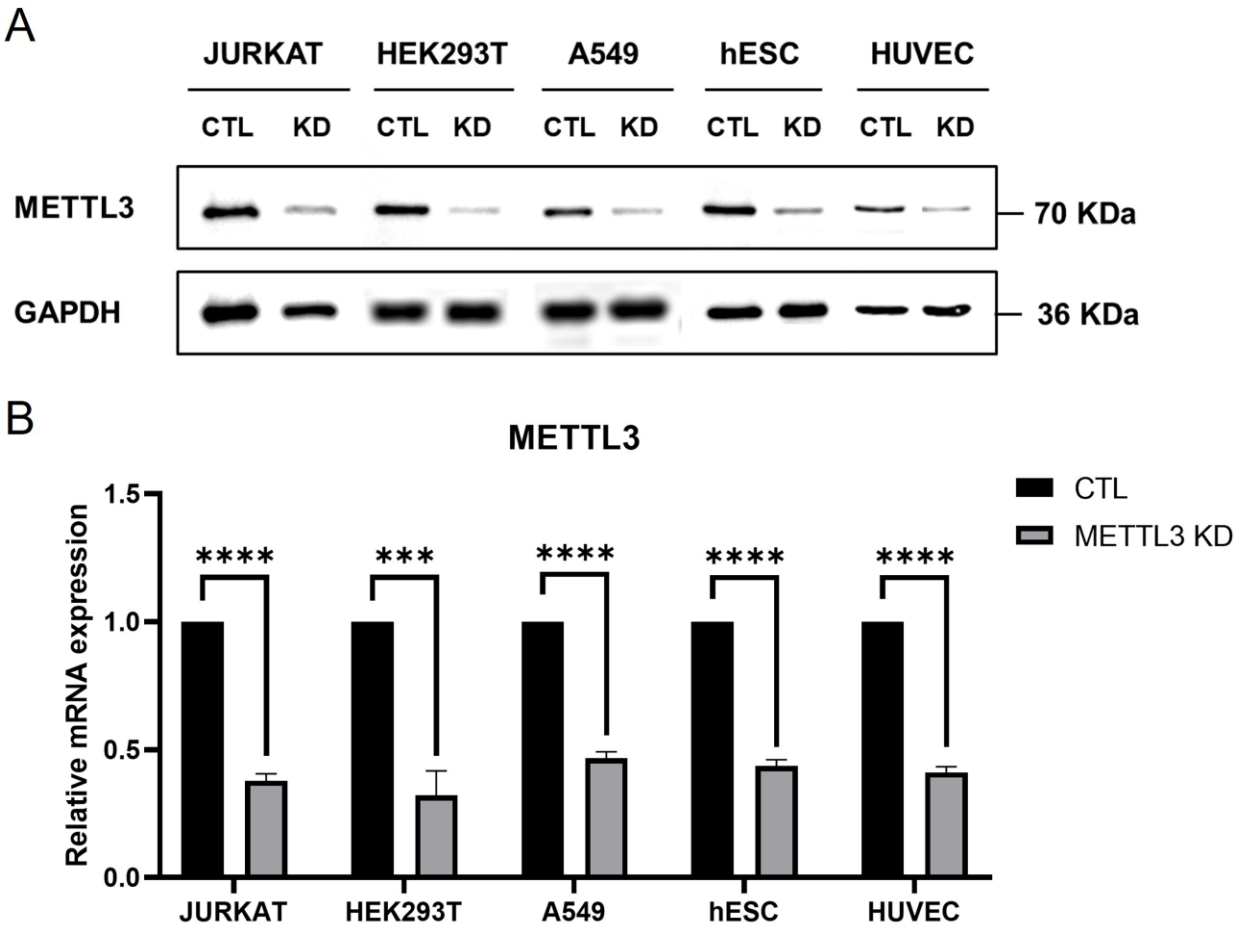

Supplementary Figure S1. Verification of *METTL3* knockdown effects.

(A) Western blot analysis for expression of METTL3 in shControl and shMETTL3 cells. (B) RT-qPCR analysis for the relative expression of *METTL3* mRNA in sh control and METTL3 KD cells. **** means $P < 0.0001$.

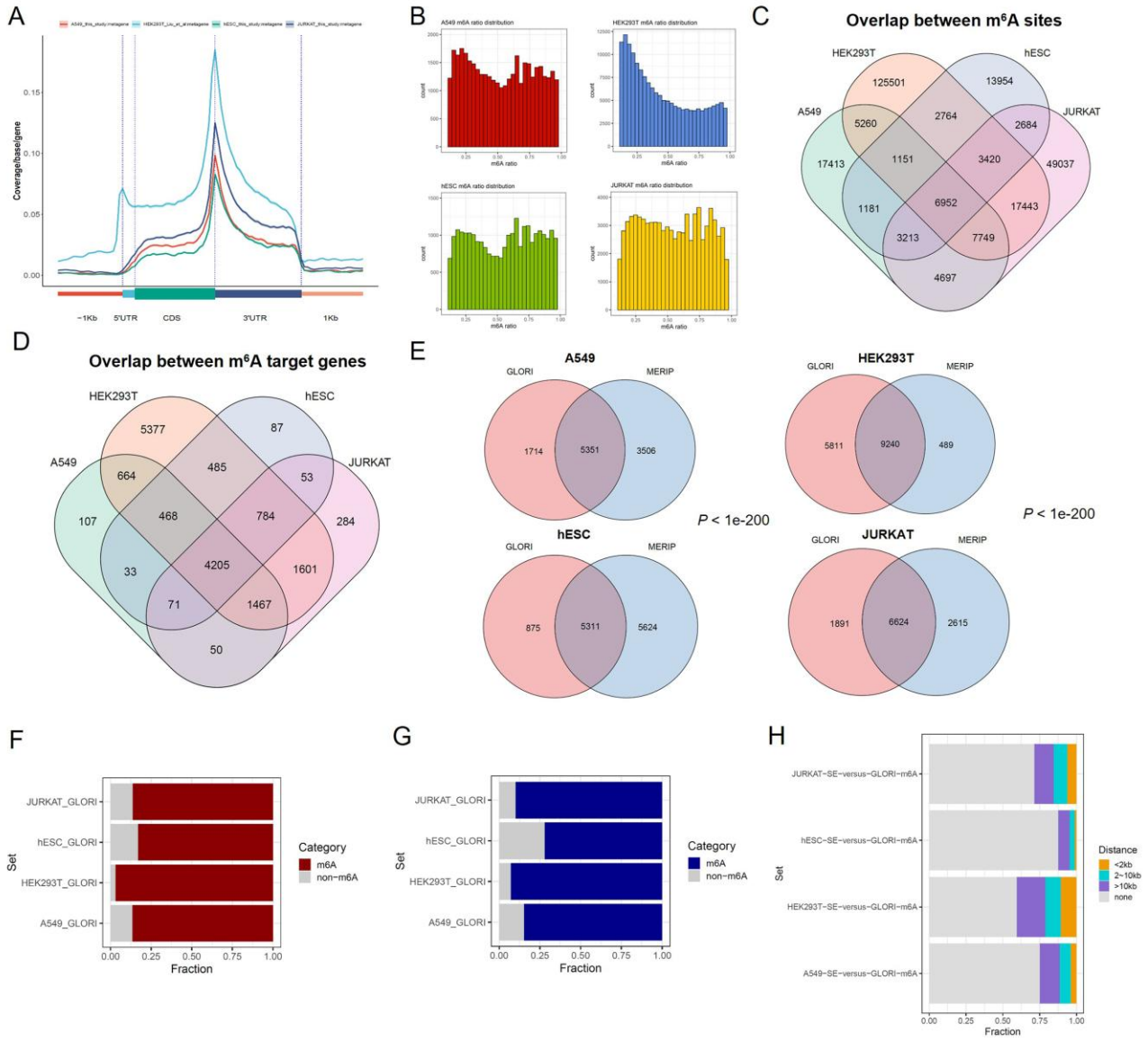

Supplementary Figure S2. Overview of m^{6}A modification sites identified by GLORI.

(A) Metagene plot showing the distribution of GLORI-identified m^{6}A modification sites in the target genes. Western blot analysis for expression of METTL3 in shControl and shMETTL3 cells. (B) Histogram illustration of m^{6}A modification ratio estimated by GLORI. (C) Venn diagram showing the overlap of m^{6}A modification sites between different cell types. (D) Venn diagram showing the overlap of m^{6}A target genes between different cell types. (E) Venn diagram showing the overlap between m^{6}A target genes identified by GLORI and those identified by MeRIP-seq in the corresponding cell types. (F) Percentage of half-life down-regulated genes with m^{6}A methylation peaks identified by GLORI on the corresponding cell types. (G) Percentage of genes showing translational efficiency changes with m^{6}A methylation peaks identified by GLORI on the corresponding cell types.

(H) Percentage of exons showing exon inclusion ratio changes with m^6A methylation sited identified by GLORI on the corresponding cell types) near their exon boundaries.

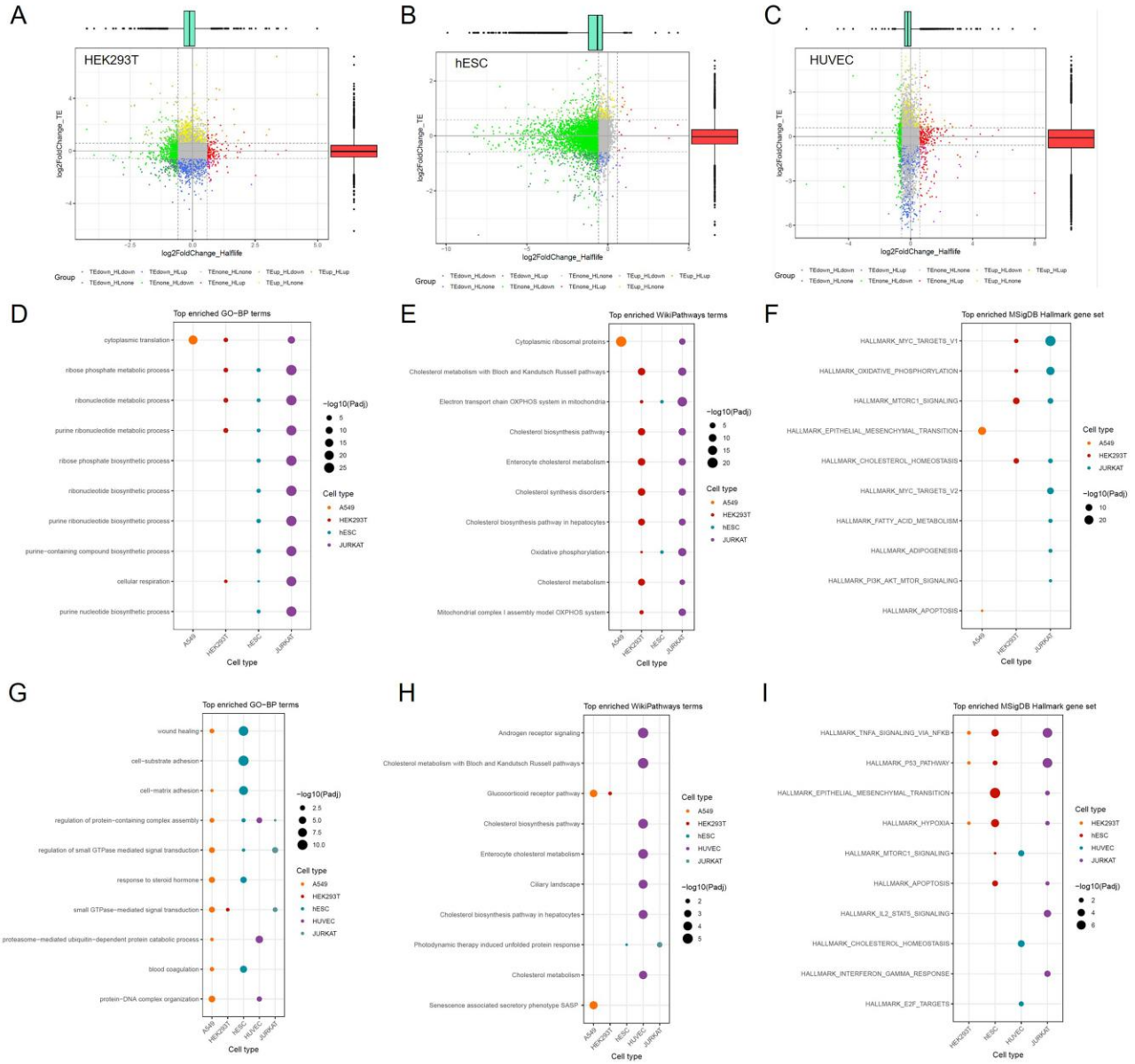

Supplementary Figure S3. Distribution and functional association of genes showing m^{6}A-mediated translational efficiency changes.

(A-C) Scatter plot showing translational efficiency versus half-life changes in HEK293T (A), hESC (B) and HUVEC cells (D) Top 10 enriched Gene Ontology-Biological Process (GO-BP) functional terms for translational efficiency down-regulated genes. (E) Top 10 enriched WikiPathways pathways for translational efficiency down-regulated genes. (F) Top 10 enriched HsigDB Hallmark gene set for translational efficiency down-regulated genes. (G-I) The corresponding results for translational efficiency up-regulated genes.

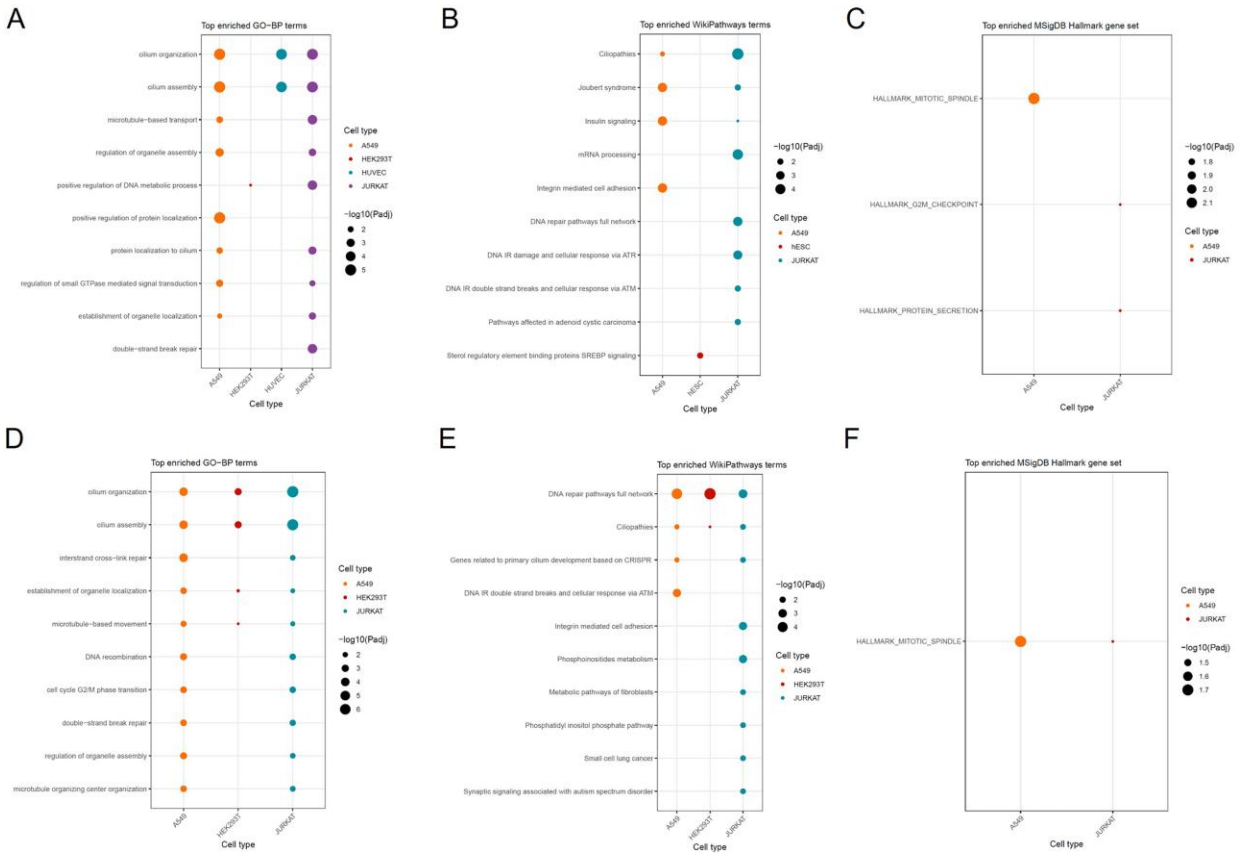

Supplementary Figure S4. Functional association of genes with exon skipping events.

(A) Top enriched GO-BP functional terms for exon inclusion ratio down-regulated genes. (B) Top enriched WikiPathways pathways for exon inclusion ratio down-regulated genes. (C) Top enriched HsigDB Hallmark gene set for exon inclusion ratio down-regulated genes. (D-F) The corresponding results for exon inclusion ratio up-regulated genes.

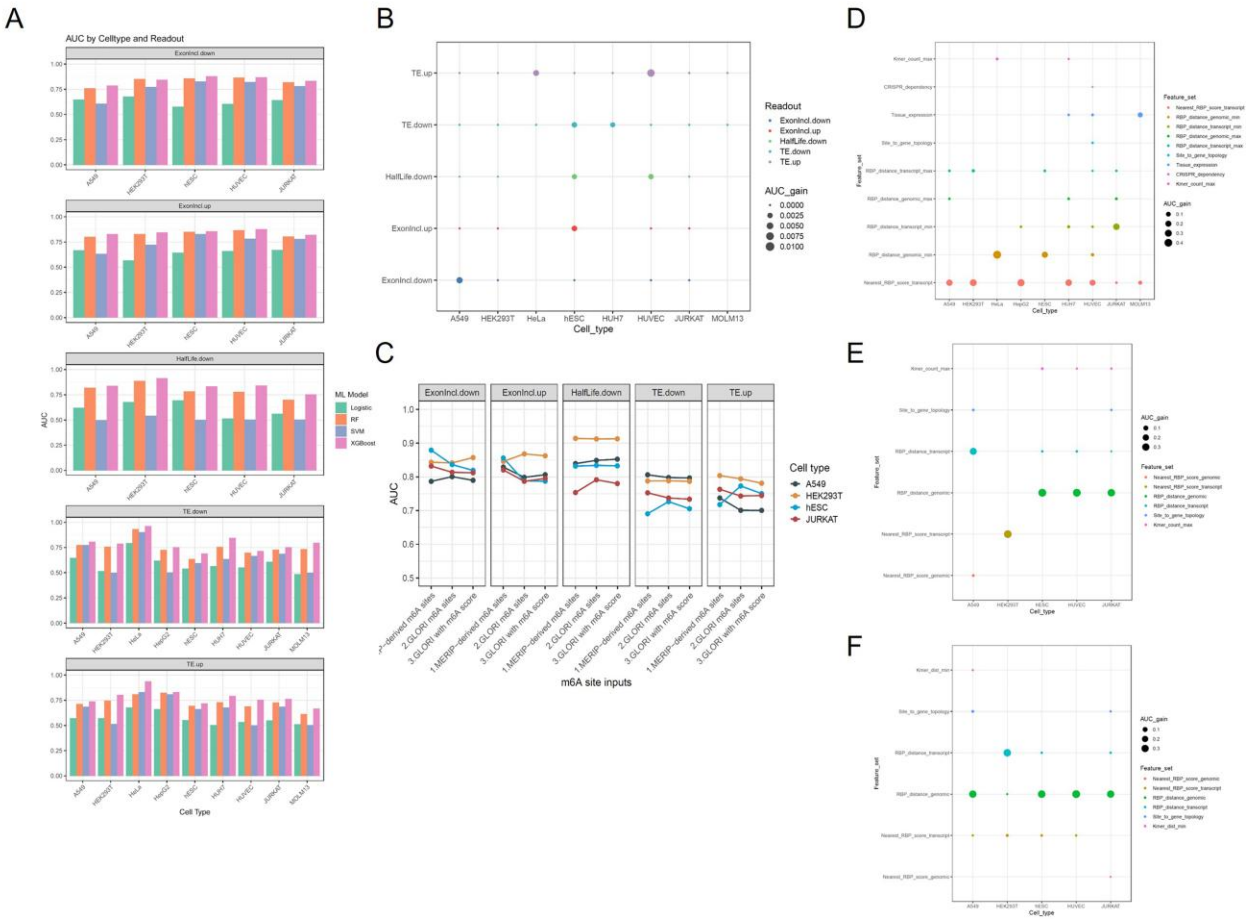

Supplementary Figure S5. Ablation experiments and feature set contribution of the machine learning predication models of m^{6}A readouts.

(A) Comparison between XGBoost and other classical machine learning models in predicting different categories of m^{6}A readouts. The classical machine learning models here include random forest (RF), logistic regression (Logistic) and support vector machine (SVM). ExonIncl means exon inclusion ratio; TE means translational efficiency. (B) Bubble plot summarizing the gain of AUC after parameter optimization of the XGBoost model. (C) Line plot comparing the performance of XGBoost models with MeRIP-seq-derived m^{6}A sites, GLORI-derived m^{6}A sites or GLORI-derived m^{6}A sites plus the corresponding m^{6}A methylation rate. (D) Bubble plot summarizing the performance contributions of different feature sets for predicting translational efficiency up-regulated genes. (E) Bubble plot summarizing the performance contributions of different feature sets for predicting exon inclusion ratio down-regulated exons. (F) Bubble plot summarizing the performance contributions of different feature sets for predicting exon inclusion ratio up-regulated exons.

1177

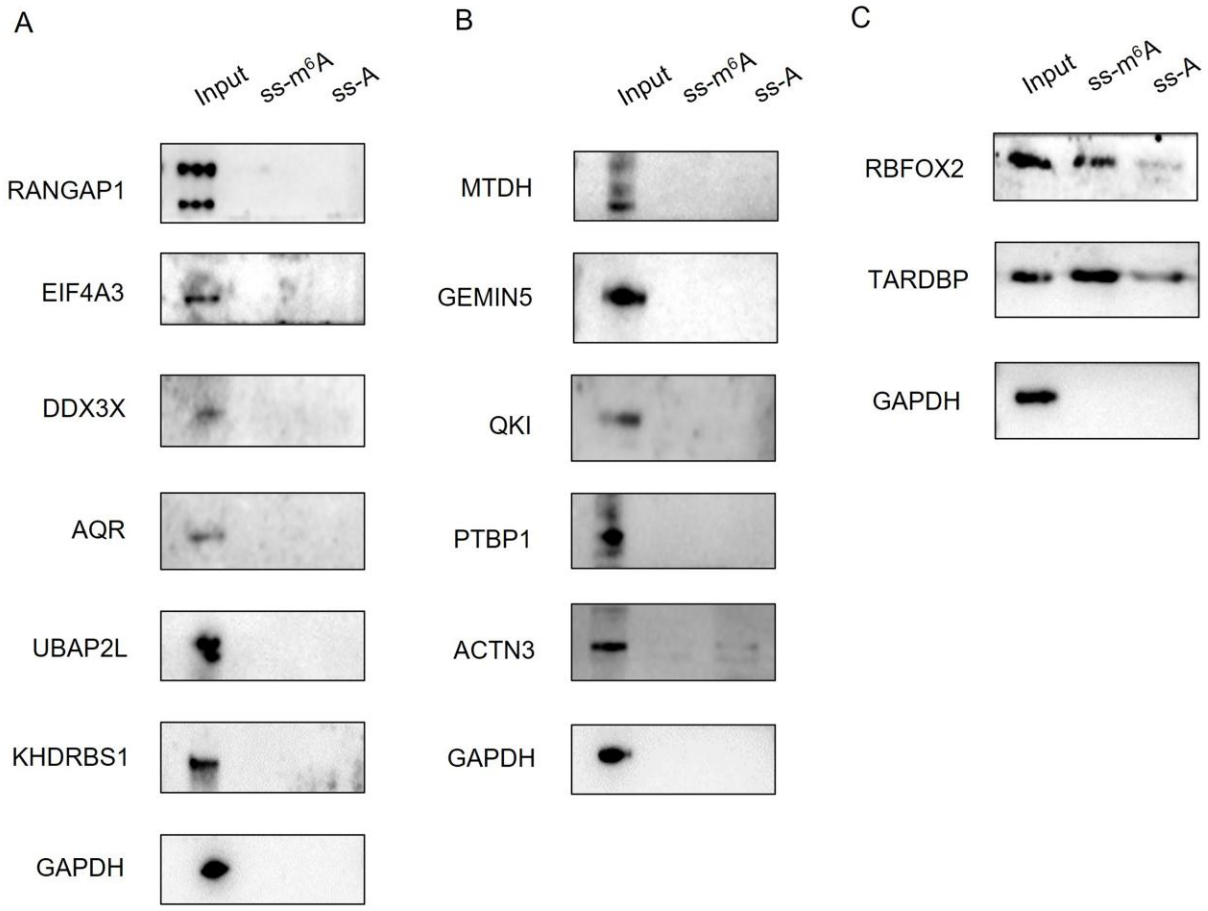

1178

1179 **Supplementary Figure S6. Screening of m^{6}A readers by RNA pull-down assay.**

1180 Three batches of RNA pull-down assay were performed. (A) RNA pull-down assay batch 1. (B) RNA
1181 pull-down assay batch 2. (C) RNA pull-down assay batch 3. RBFOX2 and TARDBP (also known as
1182 TDP43) are known m^{6}A readers that serve as positive controls here.

1183

1184

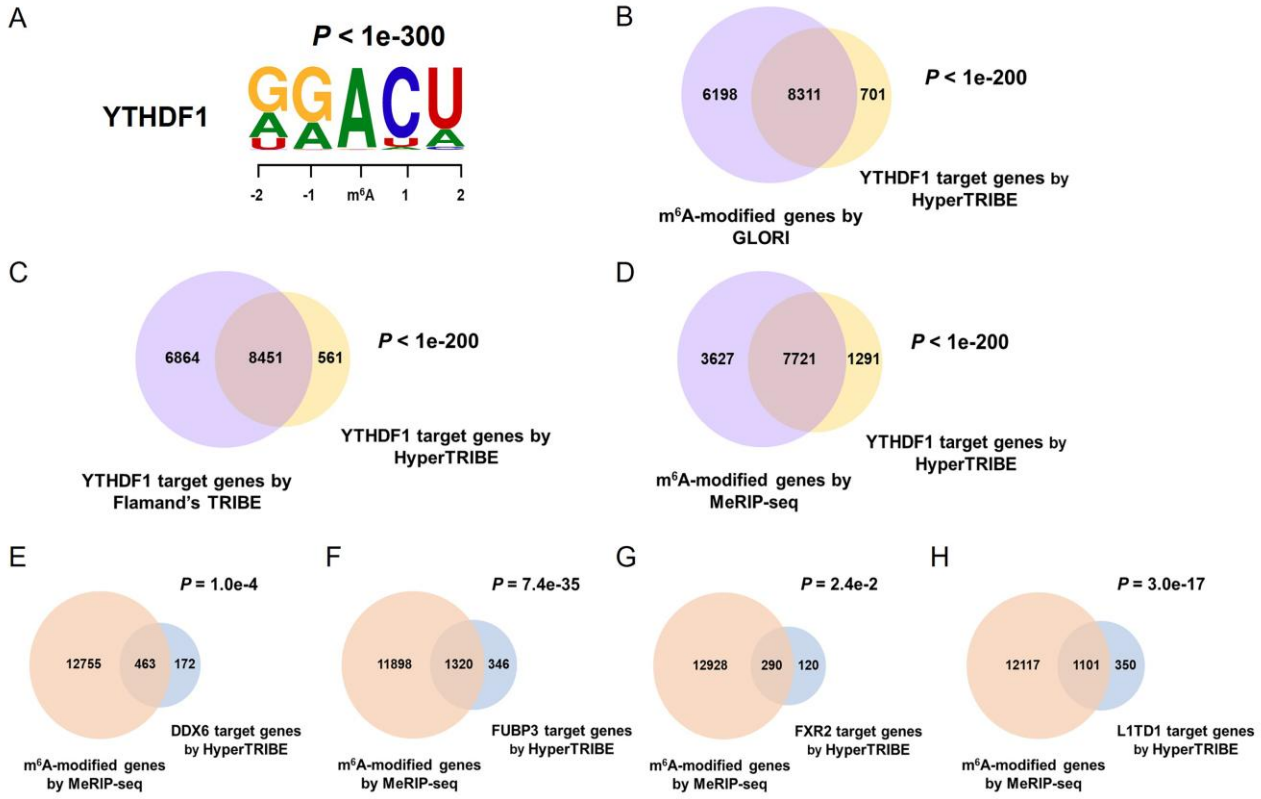

Supplementary Figure S7. Overlaps between the binding target genes of m^{6}A readers and m^{6}A modification.

HyperTRIBE assay of YTHDF1 in HEK293T was performed as the positive control assay. Then the HyperTRIBE assay was performed in hESCs for the four putative m^{6}A readers (DDX6, FUBP3, FXR2 and L1TD1) found in this study. (A) DRACH-like motifs in the proximal sequences of YTHDF1 binding sites in HEK293T. (B) Venn diagram showing the intersection between YTHDF1 target genes identified by HyperTRIBE and m^{6}A target genes identified by GLORI in HEK293T. (C) Venn diagram showing the intersection between YTHDF1 target genes identified by HyperTRIBE and those identified by Flamand et al. (D) Venn diagram showing the intersection between YTHDF1 target genes identified by HyperTRIBE and m^{6}A target genes identified by MeRIP-seq in HEK293T. (E-H) Venn diagrams showing the intersection between DDX6 (E), FUBP3 (F), FXR2 (G) and L1TD1 (H) target genes identified by HyperTRIBE and m^{6}A target genes identified by MeRIP-seq in hESC.

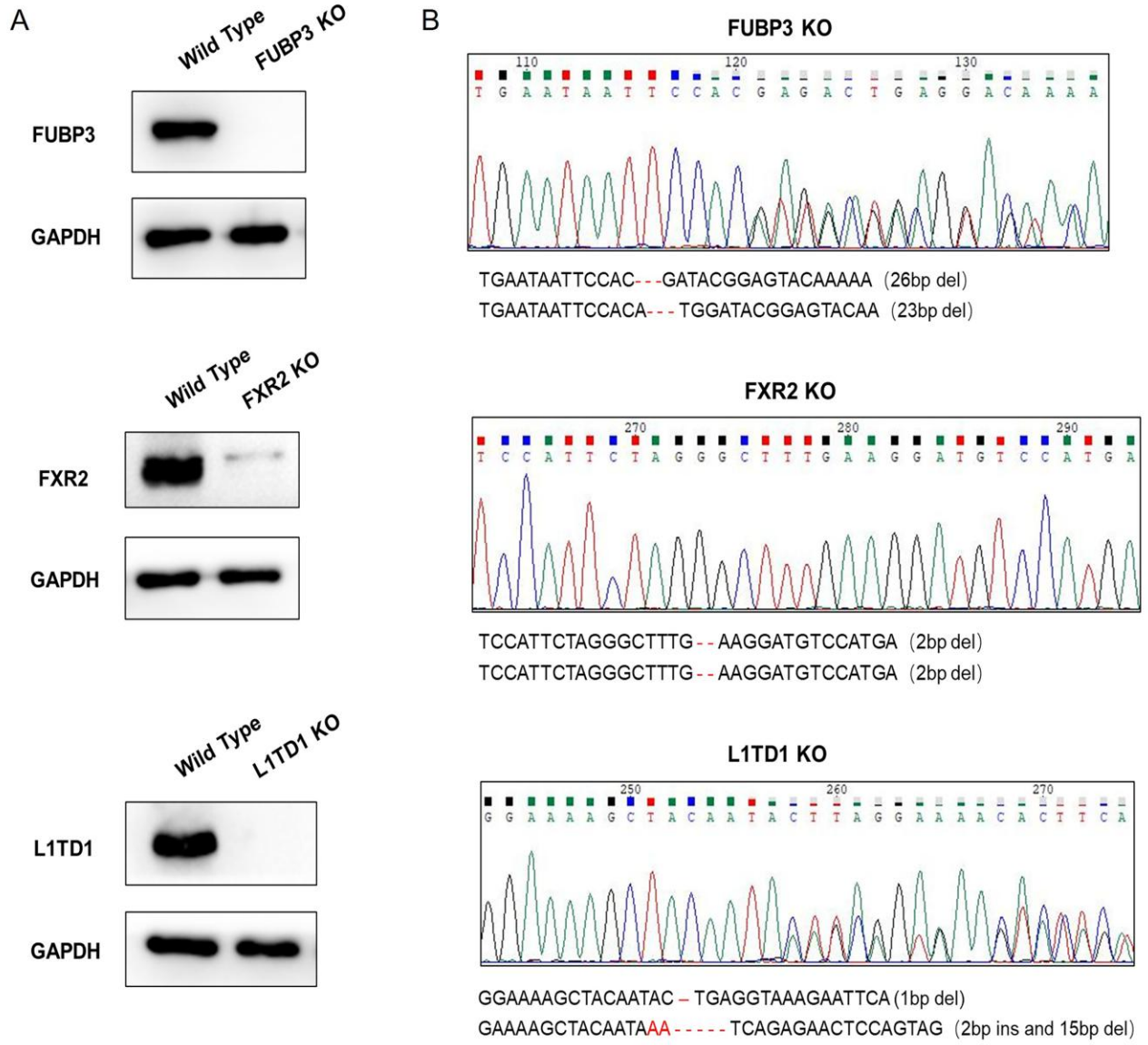

Supplementary Figure S8. Validation of *FUBP3*, *FXR2* and *L1TD1* KO cell lines by Western blot and sanger sequencing.

(A) The validation of *FUBP3*, *FXR2* and *L1TD1* KO cell lines by Western blot. (B) The validation of *FUBP3*, *FXR2* and *L1TD1* KO cell lines by sanger sequencing.

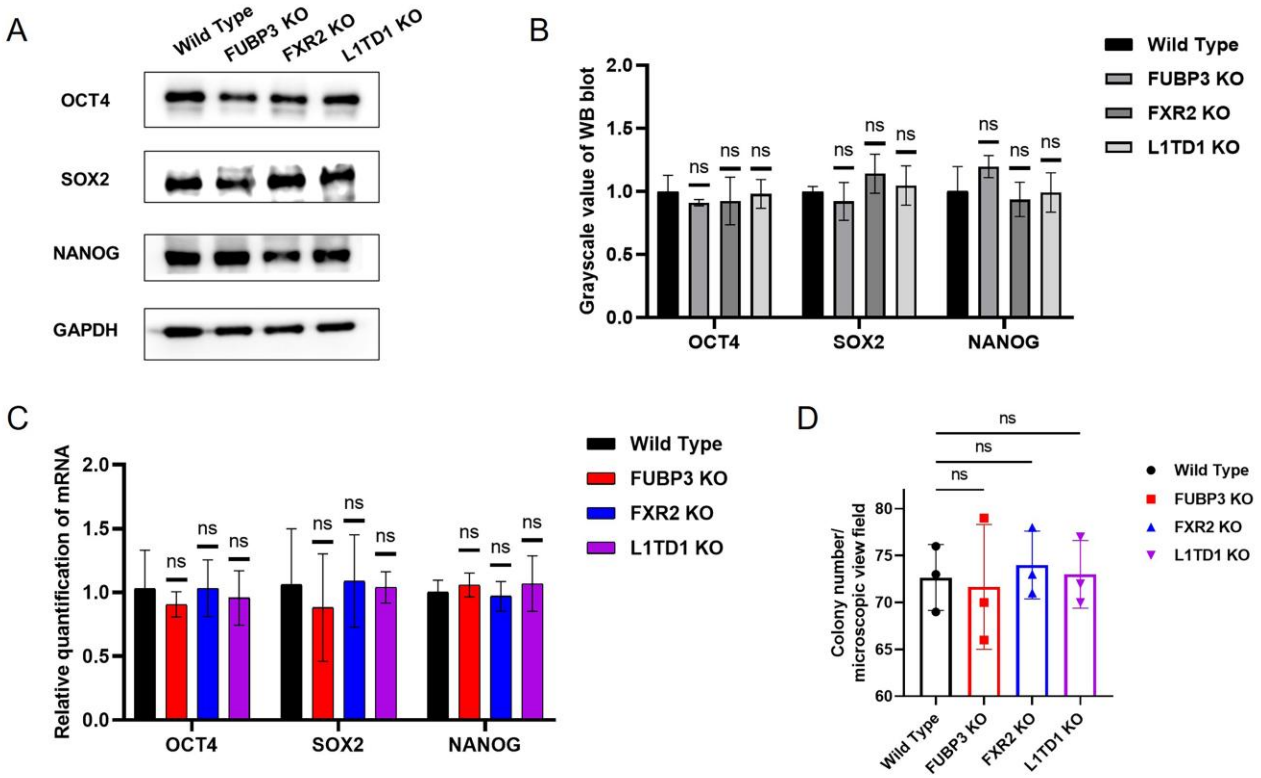

Supplementary Figure S9. Regulatory effects of m^{6}A readers on self-renewal of hESCs.

(A) Representative western blot analysis of expression of OCT4, SOX2 and NANOG in WT versus *FUBP3*, *FXR2* and *L1TD1* KO hESCs. (B) The statistics of grayscale value of western blot, ns means not significant. (C) RT-qPCR analysis of OCT4, SOX2, NANOG mRNA expression in WT versus *FUBP3*, *FXR2* and *L1TD1* KO hESCs. ns means not significant. (D) Statistics of the ALP-positive colony numbers from WT versus *FUBP3*, *FXR2* and *L1TD1* KO hESCs. ns means not significant.

Supplementary Tables

Supplementary Table S1. Oligo Sequences Synthesized Targeting METTL3.

Gene	5’	Stem	Loop	Stem	3’
METTL3	CTCGAGAAGGTATATTGCTGTTGACAGTGAGCG	ACCAAGGAACAATCCATTGTTG	TAGTGAAGCCACAGATGTA	CAACAATGGATTGTTCCTTGGC	TGCCTACTGCCTCGCAATTG

Supplementary Table S2. RT-qPCR Primers for mRNA Quantification.

Gene	Forward	Reverse
GAPDH	CTGGGCTACACTGAGCACC	AAGTGGTCGTTGAGGGCAATG
METTL3	CAAGCTGCACTTCAGACGAA	GCTTGGCGTGTGGTCTTT
OCT4	CTTGAATCCCGAATGGAAAGGG	GTGTATATCCCAGGGTGATCCTC
NANOG	ACAACTGGCCGAAGAATAGCA	GGTTCCCAGTCGGGTTCAC
SOX2	CCGTTCATCGACGAGGCTAA	ATGTGCGCGTAACTGTCCAT
TBXT (T)	TATGAGCCTCGAATCCACATAGT	CCTCGTTCTGATAAGCAGTCAC
CD34	CTACAACACCTAGTACCCTTGGA	GGTGAACACTGTGCTGATTACA
SOX17	CCTTCACGTGTACTACGGCG	GTTCAAATTCCGTGCGGTCC
SOX1	CAACCAGGACCGGGTCAAAC	CCTCGGACATGACCTTCCACT
PAX6	CGAGACTGGCTCCATCAGAC	CTTTTCGCTAGCCAGGTTGC
NES	AAGAGACTCAACAGCGACGG	TCTTGTCCCGCAGACTTCAG
FOXA2	GGAACACCACTACGCCTTCAAC	AGTGCATCACCTGTTCGTAGGC

Supplementary Table S3. Antibodies Used in This Study.

Name of Antibodies	Company	Catalog Number
GAPDH	ABclonal	AC001
METTL3	CST	86132S
OCT4	Santa cruz	sc5279
NANOG	Abcam	ab173368
SOX2	Abcam	ab171380
YTHDF1	Proteintech	17479-1-AP
YTHDC2	Proteintech	27779-1-AP
DDX6	Proteintech	14632-1-AP
FUBP3	Proteintech	10623-1-AP
FXR2	Proteintech	12552-1-AP
L1TD1	Proteintech	21528-1-AP
MTDH	Proteintech	68592-1-Ig
UBAP2L	Abcam	ab70319
AQR	ABclonal	A6011

GEMIN5	ABclonal	A17125
DDX3X	ABclonal	A5637
ACTN3	ABclonal	A12797
QKI	Proteintech	13169-1-AP
PTBP1	Proteintech	67462-1-Ig
EIF4A3	ABclonal	A8985
RANGAP1	Proteintech	67146-1-Ig
KHDRBS1	Proteintech	10222-1-AP
RBFOX2	ABclonal	A20810
TARDBP	Proteintech	10782-2-AP
HRP-conjugated anti-rabbit IgG	Beyotime	A0208
HRP-conjugated anti-mouse IgG	Beyotime	A0216

Supplementary Table S4. Public MeRIP-seq data used in this study.

Cell line	GEO ID	Cell line	GEO ID
A549	GSE76367	HeLa	GSE165690
HEK293T	GSE182607	HepG2	GSE110320
hESC	GSE52600	Huh7	GSE155413
HUVEC	GSE142386	MOLM13	GSE94613
JURKAT	GSE154035		

Supplementary Table S5. The RBP binding site profile used in this study.

RBP	Source #	Technique	Dataset ID *
AARS1	ENCODE	eCLIP	-
AATF	ENCODE	eCLIP	-
ABCF1	ENCODE	eCLIP	-
ACIN1	GEO-reanalysis	classical-CLIP	GSE81460
ACTN3	GEO-processed	eCLIP	GSE221870
ADAR	GEO-reanalysis	classical-CLIP	GSE227455, GSE161943
ADAR	GEO-processed	eCLIP	GSE227455
ADAR	ENCODE	eCLIP	-
ADAT1	ENCODE	eCLIP	-
AGGF1	ENCODE	eCLIP	-
AGO2	ENCODE	eCLIP	-
AIFM1	GEO-processed	eCLIP	GSE86035
AIMP1	GEO-processed	eCLIP	GSE117290
AKAP1	ENCODE	eCLIP	-
AKAP8	GEO-processed	seCLIP	GSE139074
AKAP8L	ENCODE	eCLIP	-
ALKBH1	POSTAR	classical-CLIP	-
ALKBH3	POSTAR, GEO-reanalysis	classical-CLIP	GSE112625
ALKBH5	POSTAR, GEO-reanalysis	classical-CLIP	GSE242283
ALYREF	POSTAR, GEO-reanalysis	classical-CLIP	GSE242283, GSE113896, GSE115429, GSE133620
APEX1	ENCODE	eCLIP	-

APOBEC3C	ENCODE	eCLIP	-
AQR	ENCODE	eCLIP	-
ATXN2	POSTAR	classical-CLIP	-
BCCIP	ENCODE	eCLIP	-
BCLAF1	ENCODE	eCLIP	-
BOLL	GEO-processed	eCLIP	GSE117290
BUD13	ENCODE	eCLIP	-
CACTIN	ENCODE	eCLIP	-
CAPRIN1	POSTAR	classical-CLIP	-
CDC40	ENCODE	eCLIP	-
CDK1	POSTAR, GEO-reanalysis	classical-CLIP	GSE100754
CELF1	GEO-processed	PIE-SEQ	GSE155844
CELF2	POSTAR	classical-CLIP	-
CELF2	GEO-processed	PIE-SEQ	GSE155844
CELF4	GEO-processed	PIE-SEQ	GSE155844
CHD7	GEO-reanalysis	classical-CLIP	GSE155844, GSE171137
CHTOP	GEO-reanalysis	classical-CLIP	GSE155844, GSE171137, GSE113896
CLK3	GEO-processed	eCLIP	GSE117290
CNBP	POSTAR	classical-CLIP	-
CNOT7	GEO-processed	eCLIP	GSE117290
CPEB4	GEO-processed	irCLIP	GSE188693
CPEB4	ENCODE	eCLIP	-
CPSF1	POSTAR	classical-CLIP	-

CPSF2	POSTAR	classical-CLIP	-
CPSF3	POSTAR	classical-CLIP	-
CPSF4	POSTAR	classical-CLIP	-
CPSF6	POSTAR	classical-CLIP	-
CPSF6	ENCODE	eCLIP	-
CPSF7	POSTAR	classical-CLIP	-
CSDE1	POSTAR, GEO-reanalysis	classical-CLIP	EMTAB3818
CSTF2	POSTAR	classical-CLIP	-
CSTF2	GEO-processed	sCLIP	GSE92995
CSTF2	ENCODE	eCLIP	-
CSTF2T	POSTAR	classical-CLIP	-
CSTF2T	ENCODE	eCLIP	-
CTCF	POSTAR, GEO-reanalysis	classical-CLIP	GSE53554
DCP1B	GEO-processed	eCLIP	GSE112782
DDX1	ENCODE	eCLIP	-
DDX21	ENCODE	eCLIP	-
DDX24	ENCODE	eCLIP	-
DDX3X	POSTAR	classical-CLIP	-
DDX3X	GEO-processed	eCLIP	GSE205536
DDX3X	ENCODE	eCLIP	-
DDX42	ENCODE	eCLIP	-
DDX43	ENCODE	eCLIP	-
DDX47	ENCODE	eCLIP	-

DDX5	GEO-processed	eCLIP	GSE115442
DDX51	ENCODE	eCLIP	-
DDX52	ENCODE	eCLIP	-
DDX54	POSTAR, GEO-reanalysis	classical-CLIP	GSE89366
DDX55	ENCODE	eCLIP	-
DDX59	ENCODE	eCLIP	-
DDX6	GEO-processed	eCLIP	GSE117290
DDX6	ENCODE	eCLIP	-
DEK	ENCODE	eCLIP	-
DGCR8	POSTAR	classical-CLIP	-
DGCR8	ENCODE	eCLIP	-
DHX30	ENCODE	eCLIP	-
DHX34	GEO-processed	seCLIP	GSE204982
DHX38	ENCODE	eCLIP	-
DICER1	POSTAR	classical-CLIP	-
DIS3	POSTAR, GEO-reanalysis	classical-CLIP	GSE64332
DIS3L2	POSTAR	classical-CLIP	-
DKC1	ENCODE	eCLIP	-
DMD	POSTAR, GEO-reanalysis	classical-CLIP	GSE128318
DROSHA	ENCODE	eCLIP	-
EED	ENCODE	eCLIP	-
EEF2	ENCODE	eCLIP	-
EFTUD2	ENCODE	eCLIP	-

EIF2B5	GEO-processed	eCLIP	GSE213867
EIF2D	GEO-processed	eCLIP	GSE213867
EIF2S2	GEO-processed	eCLIP	GSE213867
EIF3A	POSTAR	classical-CLIP	-
EIF3A	ENCODE	eCLIP	-
EIF3B	POSTAR	classical-CLIP	-
EIF3D	POSTAR	classical-CLIP	-
EIF3D	ENCODE	eCLIP	-
EIF3G	POSTAR	classical-CLIP	-
EIF3G	GEO-processed	eCLIP	GSE205536
EIF3G	ENCODE	eCLIP	-
EIF3H	ENCODE	eCLIP	-
EIF3J	GEO-processed	eCLIP	GSE213867
EIF4A3	POSTAR, GEO-reanalysis	classical-CLIP	EMTAB4000
EIF4E	POSTAR, GEO-reanalysis	classical-CLIP	EMTAB4000, GSE112276
EIF4E	ENCODE	eCLIP	-
EIF4G2	ENCODE	eCLIP	-
ELAC2	ENCODE	eCLIP	-
ELAVL1	POSTAR, GEO-reanalysis	classical-CLIP	EMTAB11854, GSE133620, GSE161943
ELAVL1	ENCODE	eCLIP	-
ESRP1	POSTAR, GEO-reanalysis	classical-CLIP	EMTAB11854, GSE133620, GSE161943, GSE233931
ESRRA	POSTAR, GEO-reanalysis	classical-CLIP	EMTAB11854, GSE133620, GSE161943, GSE233931, GSE173628
EWSR1	POSTAR	classical-CLIP	-

EWSR1	ENCODE	eCLIP	-
EXOSC10	POSTAR, GEO-reanalysis	classical-CLIP	GSE120574
EXOSC10	ENCODE	eCLIP	-
EXOSC5	ENCODE	eCLIP	-
EZH2	POSTAR	classical-CLIP	-
FAM120A	GEO-processed	eCLIP	GSE205536
FAM120A	ENCODE	eCLIP	-
FASTKD2	ENCODE	eCLIP	-
FBL	POSTAR	classical-CLIP	-
FIP1L1	POSTAR	classical-CLIP	-
FKBP4	ENCODE	eCLIP	-
FMR1	POSTAR	classical-CLIP	-
FMR1	GEO-processed	PIE-SEQ	GSE155844
FMR1	ENCODE	eCLIP	-
FTO	ENCODE	eCLIP	-
FUBP1	GEO-reanalysis	classical-CLIP	GSE155844, GSE115429
FUBP1	GEO-processed	PIE-SEQ	GSE155844
FUBP3	POSTAR, GEO-reanalysis	classical-CLIP	GSE115429
FUBP3	ENCODE	eCLIP	-
FUS	POSTAR	classical-CLIP	-
FUS	GEO-processed	eCLIP	GSE112782
FUS	ENCODE	eCLIP	-

FXR1	POSTAR	classical-CLIP	-
FXR1	ENCODE	eCLIP	-
FXR2	POSTAR	classical-CLIP	-
FXR2	ENCODE	eCLIP	-
G3BP1	POSTAR, GEO-reanalysis	classical-CLIP	GSE98856
G3BP1	ENCODE	eCLIP	-
G3BP2	POSTAR, GEO-reanalysis	classical-CLIP	GSE98856, GSE227855, GSE98856
GARS1	ENCODE	eCLIP	-
GATA2	GEO-processed	seCLIP	GSE232179
GEMIN5	POSTAR, GEO-reanalysis	classical-CLIP	GSE206967
GEMIN5	ENCODE	eCLIP	-
GINS1	POSTAR, GEO-reanalysis	classical-CLIP	GSE206967, GSE90650
GNL3	ENCODE	eCLIP	-
GPKOW	ENCODE	eCLIP	-
GRSF1	ENCODE	eCLIP	-
GRWD1	ENCODE	eCLIP	-
GTF2F1	ENCODE	eCLIP	-
HDAC9	POSTAR, GEO-reanalysis	classical-CLIP	GSE206967, GSE90650, GSE93744
HDLBP	POSTAR, GEO-reanalysis	classical-CLIP	GSE206967, GSE90650, GSE93744, GSE148259
HLTF	ENCODE	eCLIP	-
HMGB1	GEO-processed	sCLIP	GSE146047
HMGB2	GEO-processed	sCLIP	GSE146047
HNRNPA1	POSTAR, GEO-reanalysis	classical-CLIP	EMTAB3612, GSE83923

HNRNPA1	GEO-processed	eCLIP	GSE115442
HNRNPA1	ENCODE	eCLIP	-
HNRNPA2B1	POSTAR, GEO-reanalysis	classical-CLIP	GSE35799, GSE70061
HNRNPC	POSTAR	classical-CLIP	-
HNRNPC	ENCODE	eCLIP	-
HNRNPD	POSTAR	classical-CLIP	-
HNRNPF	POSTAR	classical-CLIP	-
HNRNPH1	POSTAR, GEO-reanalysis	classical-CLIP	EMTAB6220, EMTAB6221
HNRNPK	ENCODE	eCLIP	-
HNRNPL	POSTAR, GEO-reanalysis	classical-CLIP	EMTAB6220, EMTAB6221, GSE37560
HNRNPL	ENCODE	eCLIP	-
HNRNPM	POSTAR, GEO-reanalysis	classical-CLIP	GSE178223, GSE85851
HNRNPM	ENCODE	eCLIP	-
HNRNPU	POSTAR	classical-CLIP	-
HNRNPU	ENCODE	eCLIP	-
HNRNPUL1	ENCODE	eCLIP	-
HSP90AA1	GEO-processed	eCLIP	GSE221870
IFIT2	GEO-processed	eCLIP	GSE117290
IGF2BP1	POSTAR	classical-CLIP	-
IGF2BP1	GEO-processed	PIE-SEQ	GSE155844
IGF2BP1	ENCODE	eCLIP	-
IGF2BP2	POSTAR, GEO-reanalysis	classical-CLIP	GSE73847
IGF2BP2	GEO-processed	eCLIP	GSE205536

IGF2BP2	GEO-processed	eCLIP	GSE192792
IGF2BP2	GEO-processed	PIE-SEQ	GSE155844
IGF2BP2	ENCODE	eCLIP	-
IGF2BP3	POSTAR	classical-CLIP	-
IGF2BP3	ENCODE	eCLIP	-
ILF2	GEO-processed	eCLIP	GSE112782
ILF3	ENCODE	eCLIP	-
IMP3	GEO-reanalysis	classical-CLIP	GSE112782, SRP139915
INO80B	GEO-processed	eCLIP	GSE221870
KHDRBS1	GEO-processed	PIE-SEQ	GSE155844
KHDRBS1	ENCODE	eCLIP	-
KHDRBS2	GEO-processed	PIE-SEQ	GSE155844
KHDRBS3	GEO-processed	PIE-SEQ	GSE155844
KHSRP	POSTAR, GEO-reanalysis	classical-CLIP	GSE161943
KHSRP	ENCODE	eCLIP	-
L1TD1	POSTAR, GEO-reanalysis	classical-CLIP	GSE161943, GSE227855
LARP1	POSTAR, GEO-reanalysis	classical-CLIP	GSE161943, GSE227855, GSE59599
LARP4	ENCODE	eCLIP	-
LARP4B	POSTAR, GEO-reanalysis	classical-CLIP	GSE161943, GSE227855, GSE59599, GSE69169
LARP6	POSTAR, GEO-reanalysis	classical-CLIP	GSE161943, GSE227855, GSE59599, GSE69169, EMTAB9636
LARP7	ENCODE	eCLIP	-
LIN28A	POSTAR	classical-CLIP	-
LIN28A	GEO-processed	PIE-SEQ	GSE155844

LIN28B	POSTAR	classical-CLIP	-
LIN28B	GEO-processed	eCLIP	GSE205536
LIN28B	GEO-processed	PIE-SEQ	GSE155844
LIN28B	ENCODE	eCLIP	-
LSM11	ENCODE	eCLIP	-
MATR3	ENCODE	eCLIP	-
MBNL1	POSTAR, GEO-reanalysis	classical-CLIP	GSE76486
MBNL1	ENCODE	eCLIP	-
MBNL2	POSTAR	classical-CLIP	-
MCCC1	GEO-processed	eCLIP	GSE221870
METAP2	ENCODE	eCLIP	-
METTL1	POSTAR, GEO-reanalysis	classical-CLIP	GSE100754, GSE112276
METTL1	ENCODE	eCLIP	-
METTL14	POSTAR	classical-CLIP	-
METTL3	POSTAR	classical-CLIP	-
MEX3C	GEO-processed	eCLIP	GSE117290
MFAP1	ENCODE	eCLIP	-
MKRN1	GEO-reanalysis	classical-CLIP	GSE117290, GSE122869
MORC2	ENCODE	eCLIP	-
MOV10	POSTAR	classical-CLIP	-
MSI1	POSTAR, GEO-reanalysis	classical-CLIP	GSE68800
MSI2	POSTAR, GEO-reanalysis	classical-CLIP	GSE68800, GSE69583
MTDH	GEO-reanalysis	classical-CLIP	GSE117290, GSE110260

MTDH	GEO-processed	eCLIP	GSE117290
MTPAP	ENCODE	eCLIP	-
NANOS3	GEO-processed	eCLIP	GSE117290
NCBP2	ENCODE	eCLIP	-
NCBP3	POSTAR	classical-CLIP	-
NIP7	ENCODE	eCLIP	-
NIPBL	ENCODE	eCLIP	-
NKRF	ENCODE	eCLIP	-
NOL12	ENCODE	eCLIP	-
NOLC1	ENCODE	eCLIP	-
NONO	POSTAR, GEO-reanalysis	classical-CLIP	GSE114376, GSE90650
NONO	ENCODE	eCLIP	-
NOP56	POSTAR	classical-CLIP	-
NOP58	POSTAR	classical-CLIP	-
NOVA1	GEO-processed	PIE-SEQ	GSE155844
NPM1	ENCODE	eCLIP	-
NR5A1	GEO-processed	eCLIP	GSE221870
NSUN2	ENCODE	eCLIP	-
NSUN4	ENCODE	eCLIP	-
NUDT16L1	GEO-reanalysis	classical-CLIP	GSE221870, GSE118049
NUDT21	POSTAR, GEO-reanalysis	classical-CLIP	GSE161943
NUDT21	GEO-processed	eCLIP	GSE190842
NUMA1	GEO-processed	eCLIP	GSE86035

NXF1	GEO-reanalysis	classical-CLIP	GSE86035, GSE113896
OBI1	GEO-processed	eCLIP	GSE86035
PABPC4	ENCODE	eCLIP	-
PABPN1	ENCODE	eCLIP	-
PAIP1	GEO-processed	RIP	GSE150780
PARN	GEO-processed	eCLIP	GSE117290
PARP1	GEO-reanalysis	classical-CLIP	GSE117290, GSE95360
PARP1	ENCODE	eCLIP	-
PBRM1	GEO-reanalysis	classical-CLIP	GSE117290, GSE95360, GSE221619
PCBP1	GEO-reanalysis	classical-CLIP	GSE117290, GSE95360, GSE221619, GSE84700
PCBP1	ENCODE	eCLIP	-
PCBP2	ENCODE	eCLIP	-
PHC1	GEO-reanalysis	classical-CLIP	GSE117290, GSE95360, GSE221619, GSE84700, GSE103233
PHF6	ENCODE	eCLIP	-
PIAS4	GEO-processed	eCLIP	GSE221870
POLR2G	ENCODE	eCLIP	-
PPIG	ENCODE	eCLIP	-
PPIL4	ENCODE	eCLIP	-
PRDX1	GEO-processed	RIP	GSE134504
PRKRA	POSTAR	classical-CLIP	-
PRPF39	ENCODE	eCLIP	-
PRPF4	ENCODE	eCLIP	-
PRPF8	GEO-processed	eCLIP	GSE205536

PRPF8	ENCODE	eCLIP	-
PRRC2B	GEO-reanalysis	classical-CLIP	GSE205536, GSE220057
PTBP1	POSTAR, GEO-reanalysis	classical-CLIP	EMTAB5027
PTBP1	GEO-processed	eCLIP	GSE192792
PTBP1	ENCODE	eCLIP	-
PTBP3	POSTAR, GEO-reanalysis	classical-CLIP	EMTAB5027, GSE161943
PUM1	POSTAR, GEO-reanalysis	classical-CLIP	EMTAB5027, GSE161943, GSE110519, GSE115429
PUM1	ENCODE	eCLIP	-
PUM2	POSTAR, GEO-reanalysis	classical-CLIP	GSE110519
PUM2	GEO-processed	eCLIP	GSE205536
PUM2	GEO-processed	PIE-SEQ	GSE155844
PUM2	ENCODE	eCLIP	-
PUS1	ENCODE	eCLIP	-
QKI	POSTAR, GEO-reanalysis	classical-CLIP	GSE161943
QKI	GEO-processed	PIE-SEQ	GSE155844
QKI	GEO-processed	PIE-SEQ	GSE155844
QKI	ENCODE	eCLIP	-
RANGAP1	GEO-processed	eCLIP	GSE86035
RBFOX2	POSTAR, GEO-reanalysis	classical-CLIP	GSE229012, GSE85851
RBFOX2	GEO-processed	eCLIP	GSE205536
RBFOX2	ENCODE	eCLIP	-
RBM10	POSTAR, GEO-reanalysis	classical-CLIP	GSE48066
RBM12	GEO-processed	eCLIP	GSE200676

RBM15	POSTAR	classical-CLIP	-
RBM15	ENCODE	eCLIP	-
RBM15B	POSTAR	classical-CLIP	-
RBM20	GEO-processed	eCLIP	GSE176060
RBM22	ENCODE	eCLIP	-
RBM3	GEO-reanalysis	classical-CLIP	GSE176060, GSE242283, GSE241548
RBM33	GEO-reanalysis	classical-CLIP	GSE176060, GSE242283
RBM4	POSTAR, GEO-reanalysis	classical-CLIP	GSE147895
RBM45	GEO-reanalysis	classical-CLIP	GSE176060, GSE242283, GSE241548, GSE205625
RBM47	POSTAR	classical-CLIP	-
RBM5	POSTAR, GEO-reanalysis	classical-CLIP	GSE48066
RBM5	ENCODE	eCLIP	-
RBM6	POSTAR, GEO-reanalysis	classical-CLIP	GSE48066, GSE48066
RBMX	POSTAR, GEO-reanalysis	classical-CLIP	GSE48066, GSE48066, GSE114311, GSE115429, GSE74085
RBPMS	POSTAR	classical-CLIP	-
RC3H1	POSTAR, GEO-reanalysis	classical-CLIP	GSE69153
RELA	POSTAR, GEO-reanalysis	classical-CLIP	GSE69153, GSE197705
RNF187	ENCODE	eCLIP	-
RNMT	POSTAR, GEO-reanalysis	classical-CLIP	GSE69153, GSE197705, GSE112276
RO60	ENCODE	eCLIP	-
RPL29	GEO-processed	eCLIP	GSE213867
RPL35A	GEO-processed	eCLIP	GSE213867
RPS10	ENCODE	eCLIP	-

RPS11	ENCODE	eCLIP	-
RPS14	GEO-processed	eCLIP	GSE213867
RPS19	GEO-processed	eCLIP	GSE213867
RPS3	ENCODE	eCLIP	-
RPS3A	GEO-processed	eCLIP	GSE213867
RPS6	ENCODE	eCLIP	-
RTCA	GEO-processed	eCLIP	GSE232597
RTCB	POSTAR	classical-CLIP	-
RYBP	ENCODE	eCLIP	-
SAFB	ENCODE	eCLIP	-
SAFB2	ENCODE	eCLIP	-
SBDS	ENCODE	eCLIP	-
SBNO2	POSTAR, GEO-reanalysis	classical-CLIP	GSE187784
SCAF8	GEO-processed	eCLIP	GSE232597
SDAD1	ENCODE	eCLIP	-
SERBP1	POSTAR, GEO-reanalysis	classical-CLIP	EMTAB10830
SERBP1	ENCODE	eCLIP	-
SETD1A	POSTAR, GEO-reanalysis	classical-CLIP	EMTAB10830, GSE161943
SF3A1	ENCODE	eCLIP	-
SF3A3	ENCODE	eCLIP	-
SF3B1	POSTAR, GEO-reanalysis	classical-CLIP	GSE160948
SF3B1	ENCODE	eCLIP	-
SF3B4	GEO-processed	eCLIP	GSE205536

SF3B4	ENCODE	eCLIP	-
SFPQ	ENCODE	eCLIP	-
SLBP	ENCODE	eCLIP	-
SLTM	ENCODE	eCLIP	-
SMARCA4	GEO-reanalysis	classical-CLIP	GSE205536, GSE93744
SMN1	GEO-reanalysis	classical-CLIP	GSE205536, GSE93744, GSE110411
SMNDC1	ENCODE	eCLIP	-
SND1	ENCODE	eCLIP	-
SNIP1	GEO-reanalysis	classical-CLIP	GSE205536, GSE93744, GSE110411, GSE181777
SNRNP200	ENCODE	eCLIP	-
SNRPA	GEO-processed	eCLIP	GSE117290
SNRPA1	ENCODE	eCLIP	-
SNRPC	ENCODE	eCLIP	-
SNRPD3	ENCODE	eCLIP	-
SORBS2	GEO-processed	RIP	GSE100323
SRRM4	POSTAR	classical-CLIP	-
SRSF1	POSTAR, GEO-reanalysis	classical-CLIP	GSE130867, GSE131745, GSE71096, GSE83923
SRSF1	GEO-processed	PIE-SEQ	GSE155844
SRSF1	ENCODE	eCLIP	-
SRSF10	POSTAR, GEO-reanalysis	classical-CLIP	GSE71096
SRSF2	GEO-reanalysis	classical-CLIP	GSE155844, GSE111900, GSE207643
SRSF2	GEO-processed	PIE-SEQ	GSE155844
SRSF3	GEO-reanalysis	classical-CLIP	GSE155844, GSE71096

SRSF3	GEO-processed	PIE-SEQ	GSE155844
SRSF5	ENCODE	eCLIP	-
SRSF7	POSTAR, GEO-reanalysis	classical-CLIP	GSE71096
SRSF7	ENCODE	eCLIP	-
SRSF9	POSTAR, GEO-reanalysis	classical-CLIP	GSE71096
SRSF9	ENCODE	eCLIP	-
SSB	POSTAR	classical-CLIP	-
SSB	ENCODE	eCLIP	-
STAU1	POSTAR	classical-CLIP	-
STAU2	GEO-processed	eCLIP	GSE232597
STAU2	GEO-processed	PIE-SEQ	GSE155844
STAU2	ENCODE	eCLIP	-
SUB1	ENCODE	eCLIP	-
SUGP2	ENCODE	eCLIP	-
SUPV3L1	ENCODE	eCLIP	-
TAF15	POSTAR	classical-CLIP	-
TAF15	ENCODE	eCLIP	-
TARBP2	POSTAR	classical-CLIP	-
TARDBP	POSTAR, GEO-reanalysis	classical-CLIP	EMTAB4733, GSE85851
TARDBP	GEO-processed	PIE-SEQ	GSE155844
TARDBP	ENCODE	eCLIP	-
TBRG4	POSTAR, GEO-reanalysis	classical-CLIP	GSE156556
TBRG4	ENCODE	eCLIP	-

TENT4B	POSTAR, GEO-reanalysis	classical-CLIP	GSE156556, GSE36987
TIA1	POSTAR	classical-CLIP	-
TIA1	GEO-processed	eCLIP	GSE166402
TIA1	ENCODE	eCLIP	-
TIAL1	POSTAR	classical-CLIP	-
TIAL1	ENCODE	eCLIP	-
TNRC6A	POSTAR	classical-CLIP	-
TNRC6B	POSTAR	classical-CLIP	-
TNRC6C	POSTAR	classical-CLIP	-
TOB1	GEO-processed	eCLIP	GSE117290
TOB2	GEO-processed	eCLIP	GSE117290
TRA2A	ENCODE	eCLIP	-
TRIM25	GEO-reanalysis	classical-CLIP	GSE117290, GSE104949
TRMT10A	GEO-reanalysis	classical-CLIP	GSE117290, GSE104949, GSE146207
TRNAU1AP	GEO-processed	eCLIP	GSE232597
TRUB1	GEO-reanalysis	classical-CLIP	GSE232597, GSE143510
TXN	GEO-processed	RIP	GSE212595
U2AF1	POSTAR, GEO-reanalysis	classical-CLIP	GSE203531
U2AF1	ENCODE	eCLIP	-
U2AF2	POSTAR, GEO-reanalysis	classical-CLIP	GSE83923, GSE99688
U2AF2	ENCODE	eCLIP	-
UBAP2L	GEO-processed	eCLIP	GSE117290
UCHL5	ENCODE	eCLIP	-

UPF1	POSTAR	classical-CLIP	-
UPF1	ENCODE	eCLIP	-
UTP18	ENCODE	eCLIP	-
UTP3	ENCODE	eCLIP	-
VIM	GEO-processed	eCLIP	GSE86035
WDR3	ENCODE	eCLIP	-
WDR33	POSTAR	classical-CLIP	-
WDR4	POSTAR, GEO-reanalysis	classical-CLIP	GSE112276
WDR43	ENCODE	eCLIP	-
WRN	ENCODE	eCLIP	-
WTAP	POSTAR	classical-CLIP	-
XPO5	POSTAR, GEO-reanalysis	classical-CLIP	GSE111964
XPO5	ENCODE	eCLIP	-
XRCC6	ENCODE	eCLIP	-
XRN2	ENCODE	eCLIP	-
YBX1	POSTAR, GEO-reanalysis	classical-CLIP	GSE111964, GSE133620, GSE150925, GSE249896
YBX3	ENCODE	eCLIP	-
YTHDC1	POSTAR, GEO-reanalysis	classical-CLIP	GSE71096, GSE74397
YTHDC1	GEO-processed	PIE-SEQ	GSE155844
YTHDC2	POSTAR	classical-CLIP	-
YTHDC2	GEO-processed	PIE-SEQ	GSE155844
YTHDF1	POSTAR	classical-CLIP	-
YTHDF1	GEO-processed	STAMP	GSE200712

YTHDF1	GEO-processed	TRIBE	GSE200712
YTHDF1	GEO-processed	PIE-SEQ	GSE155844
YTHDF2	POSTAR	classical-CLIP	-
YTHDF2	GEO-processed	STAMP	GSE200712
YTHDF2	GEO-processed	TRIBE	GSE200712
YTHDF2	GEO-processed	PIE-SEQ	GSE155844
YTHDF3	POSTAR	classical-CLIP	-
YTHDF3	GEO-processed	STAMP	GSE200712
YTHDF3	GEO-processed	TRIBE	GSE200712
YWHAE	GEO-processed	eCLIP	GSE221870
YWHAG	GEO-processed	eCLIP	GSE221870
YWHAG	ENCODE	eCLIP	-
YWHAH	GEO-processed	eCLIP	GSE221870
YWHAZ	GEO-processed	eCLIP	GSE221870
ZC3H11A	GEO-processed	eCLIP	GSE205536
ZC3H11A	ENCODE	eCLIP	-
ZC3H7B	POSTAR	classical-CLIP	-
ZC3H8	ENCODE	eCLIP	-
ZC3HAV1	GEO-processed	eCLIP	GSE215250
ZCCHC4	GEO-reanalysis	classical-CLIP	GSE215250, GSE102336, GSE188703
ZFP36	GEO-reanalysis	classical-CLIP	GSE215250, GSE102336, GSE188703, GSE53184
ZFP36L1	GEO-reanalysis	classical-CLIP	GSE215250, GSE102336, GSE188703, GSE53184, GSE215769
ZNF184	GEO-processed	eCLIP	GSE86035

ZNF622	ENCODE	eCLIP	-
ZNF800	ENCODE	eCLIP	-
ZRANB2	ENCODE	eCLIP	-
ZRSR2	GEO-reanalysis	classical-CLIP	GSE86035, GSE203531

For ENCODE data, two profiles were prepared for each RBP, i.e., 1) merged with default pipeline and 2) merged by taking union of the two biological replicates.

* The dataset ID recorded in POSTAR or ENCODE are not listed, as these IDs are publicly available in the corresponding databases.